MMR **MILITARY MEDICAL RESEARCH**

Single-cell transcriptomic dissection of the cellular and molecular events underlying the triclosan-induced liver fibrosis in mice

Yun-Meng Bai[1†], Fan Yang[2,3†], Piao Luo[2†], Lu-Lin Xie[2†], Jun-Hui Chen[1], Yu-Dong Guan[2], Hong-Chao Zhou[2], Teng-Fei Xu[2], Hui-Wen Hao[2], Bing Chen[2,3], Jia-Hui Zhao[2,3], Cai-Ling Liang[2], Ling-Yun Dai[1,2*], Qing-Shan Geng[1,2*] and Ji-Gang Wang[1,2,4,5,6*] [ID]

Abstract

Background Triclosan [5-chloro-2-(2,4-dichlorophenoxy) phenol, TCS], a common antimicrobial additive in many personal care and health care products, is frequently detected in human blood and urine. Therefore, it has been considered an emerging and potentially toxic pollutant in recent years. Long-term exposure to TCS has been suggested to exert endocrine disruption effects, and promote liver fibrogenesis and tumorigenesis. This study was aimed at clarifying the underlying cellular and molecular mechanisms of hepatotoxicity effect of TCS at the initiation stage.

Methods C57BL/6 mice were exposed to different dosages of TCS for 2 weeks and the organ toxicity was evaluated by various measurements including complete blood count, histological analysis and TCS quantification. Single cell RNA sequencing (scRNA-seq) was then carried out on TCS- or mock-treated mouse livers to delineate the TCS-induced hepatotoxicity. The acquired single-cell transcriptomic data were analyzed from different aspects including differential gene expression, transcription factor (TF) regulatory network, pseudotime trajectory, and cellular communication, to systematically dissect the molecular and cellular events after TCS exposure. To verify the TCS-induced liver fibrosis, the expression levels of key fibrogenic proteins were examined by Western blotting, immunofluorescence, Masson's trichrome and Sirius red staining. In addition, normal hepatocyte cell MIHA and hepatic stellate cell LX-2 were used as in vitro cell models to experimentally validate the effects of TCS by immunological, proteomic and metabolomic technologies.

Results We established a relatively short term TCS exposure murine model and found the TCS mainly accumulated in the liver. The scRNA-seq performed on the livers of the TCS-treated and control group profiled the gene expressions of > 76,000 cells belonging to 13 major cell types. Among these types, hepatocytes and hepatic stellate cells (HSCs) were significantly increased in TCS-treated group. We found that TCS promoted fibrosis-associated proliferation of hepatocytes, in which Gata2 and Mef2c are the key driving TFs. Our data also suggested that TCS induced the

---

†Yun-Meng Bai, Fan Yang, Piao Luo, and Lu-Lin Xie contributed equally to this work

*Correspondence:
Ling-Yun Dai
dai.lingyun@szhospital.com
Qing-Shan Geng
gengqingshan@gdph.org.cn
Ji-Gang Wang
jgwang@icmm.ac.cn
Full list of author information is available at the end of the article

Bai *et al. Military Medical Research*   (2023) 10:7

Page 2 of 22

proliferation and activation of HSCs, which was experimentally verified in both liver tissue and cell model. In addition, other changes including the dysfunction and capillarization of endothelial cells, an increase of fibrotic characteristics in B plasma cells, and M2 phenotype-skewing of macrophage cells, were also deduced from the scRNA-seq analysis, and these changes are likely to contribute to the progression of liver fibrosis. Lastly, the key differential ligand-receptor pairs involved in cellular communications were identified and we confirmed the role of GAS6_AXL interaction-mediated cellular communication in promoting liver fibrosis.

Conclusions TCS modulates the cellular activities and fates of several specific cell types (including hepatocytes, HSCs, endothelial cells, B cells, Kupffer cells and liver capsular macrophages) in the liver, and regulates the ligand-receptor interactions between these cells, thereby promoting the proliferation and activation of HSCs, leading to liver fibrosis. Overall, we provide the first comprehensive single-cell atlas of mouse livers in response to TCS and delineate the key cellular and molecular processes involved in TCS-induced hepatotoxicity and fibrosis.

Keywords Triclosan, scRNA-seq, Liver fibrogenesis, Hepatic stellate cell

Background

Triclosan (TCS) is an antimicrobial agent that has been widely used worldwide for approximately 50 years since its first introduction in hospital settings [1, 2]. Although TCS has been banned from use in consumer antiseptic soap and hand sanitizer products by the US Food and Drug Administration (FDA) [3], it remains present in many readily accessible consumer products for daily use, such as toothpaste, mouthwash, shampoo, deodorant and cosmetics [4]. TCS is commonly added at a concentration of 3.5–17.0 mmol/L (i.e., 0.1–0.5%) [5]. Depending on the exposure route, TCS is absorbed into the human body through the skin or oral mucosa, and is detectable in human urine, nails, blood and breast milk [6, 7]. A recent study in China has reported detectable TCS in the urine and nails of 69–80% of participants [8]. The levels of TCS in the human body differ depending on the exposure sites, concentration/amount of exposure and type of exposure. Exposure to TCS-containing toothpaste for 14 d has been found to increase the TCS plasma concentration from 0.009–0.81 to 26–296 ng/g [9]. Use of 15 ml mouthwash containing as little as 0.03% TCS twice daily has been found to result in a plasma concentration of TCS plateauing at 74.5–94.2 ng/ml within as little as 2 d [10]. In humans, the liver is the main organ of TCS accumulation and metabolism [11]. TCS present at low levels is quickly detoxified by glucuronidation and sulfonation through catalysis by glucuronosyltransferases and sulfotransferases [12]. The potential risks of TCS on human health have drawn the public's attention, and have been a subject of active debate and study in recent years [4, 13–15].

Long-term exposure to TCS may potentially cause various disorders, including gut microbiome impairment [16], induction of colonic inflammation and colitis-associated colon tumorigenesis [17], neurobehavioral toxicity [18, 19] and increased incidence of bone diseases [20].

The hepatotoxicity of long-term exposure of TCS has also been reported, thus promoting not only nonalcoholic steatohepatitis (NASH) but also liver tumorigenesis [21, 22]. TCS-induced hepatotoxicity has been attributed to the activation of constitutive androstane receptor and peroxisome proliferator activated receptor α (PPARα), and the promotion of liver fibrogenesis [23, 24]. Months-long TCS exposure has been found to impair lipid homeostasis and accelerate liver damage in mice [25]. However, the underlying cellular and molecular mechanisms of hepatotoxicity induced by TCS exposure, particularly at the initiation stage, remain largely unknown.

In contrast to traditional bulk RNA sequencing, single cell RNA sequencing (scRNA-seq) can unveil the transcriptional heterogeneity of cells and tissues with high accuracy and reproducibility [26]. This technique has been used in deciphering the toxicity profiling of many hazardous substances in humans and other animals [27, 28]. In addition, scRNA-seq has been used in studies of liver diseases, including liver cirrhosis [29], NASH [30] and hepatocellular carcinoma [31]. The cellular landscape of the liver has also been recently described by scRNA-seq [32].

In this study, a relatively short-term TCS exposure mouse model was established. To explore the potential hepatotoxicity mechanism of TCS at the single cell level, we used scRNA-seq to comprehensively profile the changes in gene expression and the modulation of different cell types in the liver of these mice.

Methods

Animals and drug treatment

All animal experimental procedures were approved by the Animal Care and Use Committee at Shenzhen People's Hospital (No. AUP-210901-DLY-0001-01). Eighteen male C57BL/6 mice (5 weeks old) were purchased from

Bai *et al. Military Medical Research*   (2023) 10:7

Page 3 of 22

GemPharmatech (Guangdong, China) and maintained for 7 d for adaption. The mice were randomly divided into three groups (control, TCS-100 and TCS-200, with 6 mice per group), which were treated with corn oil, 100 mg/(kg·d) or 200 mg/(kg·d) TCS, respectively, for 14 d via intragastric administration. TCS was dissolved in corn oil at a concentration of 20 mg/ml or 40 mg/ml. Afterward, the mice were anesthetized, and blood samples were collected for routine testing, and serum and biochemical analyses. The mice were perfused with PBS followed by organ weighing and collection. The liver tissues were dissected to perform scRNA-seq and histological analysis, and the remaining tissues were frozen in liquid nitrogen and stored at -80 °C.

Measurement of TCS concentration
The metabolites in serum and liver tissue samples were extracted with methanol. TCS standards were prepared at gradient concentrations of 5, 10, 50, 100, 500 and 1000 ng/ml. All the standards and extracted samples were measured in triplicate by liquid chromatography tandem-mass spectrometry (LC–MS/MS). The areas under the curve of the extracted ion chromatogram of TCS were integrated to represent the level of TCS. The standard curve was plotted with the different concentrations of TCS standards, and TCS concentrations in serum or liver samples were calculated.

Histological analysis
For histological analysis, a portion of the liver was fixed in 4% paraformaldehyde and embedded in paraffin. After tissues were cut into sections, histological changes were evaluated with hematoxylin and eosin (H&E) staining. For evaluation of the hepatic collagen content and assessment of the degree of fibrosis, the paraffin-embedded liver sections were also stained with Masson's trichrome and Sirius red.

Cell culture and treatment
LX-2 (Procell, China) and MIHA (Syngene, China) cells were cultured in DMEM with 10% fetal bovine serum and 1% penicillin/streptomycin in a 5% CO_2 incubator at 37 °C. For RNA interference experiments, 100 nmol/L siRNA was transfected into cells with Lipofectamine 3000 (Thermo, USA). Cell viability was determined by cell counting kit-8 (CCK-8) reagent according to the manufacturer's instructions at the appropriate time points as specified in the paper. LX-2 cells were also treated with 10 or 20 μmol/L TCS for 24 h, then subjected to immunological analysis. In addition, BGB324 (MedChemExpress, USA) and recombinant growth arrest specific 6 (rGAS6) protein (MedChemExpress, USA) were used to treat LX-2 cells under the indicated conditions.

Western blotting
For western blotting, a portion of frozen liver was dissected and ground in liquid nitrogen. The proteins were extracted with RIPA lysis buffer (#P0013B, Beyotime, China) supplemented with 1× Protease Inhibitor Cocktail (#P8849, Sigma, USA). Protein concentrations were determined by Pierce™ BCA Protein Assay Kit (#23225, Thermo, USA). Equal amounts of proteins from different mice liver samples were separated by SDS-PAGE and transferred to PVDF membranes. The membranes were then blocked with 5% skim milk in TBST for 1 h and incubated with primary antibodies overnight at 4 °C. The antibodies included anti-alpha smooth muscle actin (α-SMA) [1:1000; #19245s, Cell Signaling Technology (CST), USA], anti-phospho-Akt (Thr308) (1:1000; #13038S, CST, USA), anti-pan-Akt (1:1000; #4691T, CST, USA) and anti-GAPDH (1:50,000; #60004-1-Ig, Proteintech, China), and corresponding secondary antibody was incubated with membrane for 1 h after washed thrice with TBST. The protein bands were then washed thrice with TBST and visualized with Clarity Western ECL Substrate (#170-5061, Bio-Rad, USA) by using G:BOX Chemi XX9 (Syngene, UK) and semi-quantitative analysis was performed by ImageJ (National Institutes of Health, USA).

Immunofluorescence
The frozen mouse liver tissue embedded in O.C.T. (#4583, SAKURA, Japan) was cut into 10 μm thick sections. The sections were fixed with acetone/methanol (4:1) for 10 min at -20 °C, washed with TBS twice and blocked with 4% donkey serum for 1 h at room temperature (RT). Sections were then incubated with the indicated primary antibodies, including rabbit anti-collagen I (1:100; #PAB13488, Abnova, Taiwan, China), rabbit anti-GAS6 (1:200; #13795-1-AP, Proteintech, China), rabbit anti-integrin subunit beta 1 (ITGB1) (1:200; #26918-1-AP, Proteintech, China), rat anti-CD68 (1:100; #14-0681-82, eBioscience, USA), rabbit anti-desmin (DES) (1:200; #16520-1-AP, Proteintech, China) and rabbit anti-lymphatic vessel endothelial hyaluronan receptor 1 (LYVE1) (1:100; #ab281587, Abcam, UK) at RT for 1 h. After being washed with TBST thrice, the sections were then incubated with corresponding Donkey anti-Rat/Rabbit Alexa Fluor 488/594-conjugated secondary antibodies (1:1000; #A-21206-21209, Thermo, USA) for 1 h at RT. Finally, the sections were counterstained and mounted with DAPI, and observed with fluorescence microscopy.

Preparation of single cell suspension
Samples from the mice from control and TCS-200 groups were subjected to scRNA-seq analysis. Briefly,

Bai *et al. Military Medical Research*   (2023) 10:7

Page 4 of 22

three liver samples from each group were dissected and cut into small pieces, followed by dissociation using the Liver Dissociation Kit for mouse (Miltenyi Biotec, Germany). The dissociated cell solution was then filtered through a 70-μm cell strainer (Greiner, Germany) and rinsed with 15 ml DMEM. The cells were pelleted by centrifugation at 300 *g* for 10 min, followed by resuspending with 1 ml PBS. Subsequently, 10 ml of $1 \times$ Red Blood Cell Lysis Solution (Miltenyi Biotec, Germany) was added to lyse red blood cells. Samples were then washed with PBS twice to obtain single-cell suspensions.

scRNA-seq and data preprocessing

The single-cell suspensions were used for scRNA-seq library construction with the Single Cell 3′ Reagent Kit v3.1 (10× Genomics) according to the manufacturer's instructions. The constructed libraries were sequenced on the Illumina HiseqXTEN platform.

The Cell Ranger Software Suite (v6.1.1) was used to perform sample de-multiplexing, barcode processing and single-cell 3′ unique molecular identifier (UMI) counting with the mm10 reference mouse genome obtained from Ensembl. Specifically, Spliced Transcripts Alignment to a Reference (STAR) was used for FASTQ alignment. Cell barcodes were then automatically determined on the basis of the distribution of the UMI count. Finally, the gene-barcode matrix of all six samples was integrated with Seurat (v4.0.3) to remove batch effects. Quality control was first performed independently to identify appropriate thresholds for each individual sample. Gene-barcode matrices for each sample generated by Cell Ranger were loaded into R (https://www.r-project.org/) as a Seurat object for filtering, data normalization, dimension reduction, clustering and differentially expressed gene (DEGs) analysis. Genes were excluded if they were detectable in fewer than three cells. The following criteria were then applied to each cell: gene number between 200 and 5000; UMI count between 500 and 20,000; and mitochondrial gene percentage below 0.15 or 0.25. After filtering, a total of 76,209 cells (37,841 for the control group and 38,368 for TCS-200 group) remained for further analysis.

Next, *SCTransform* was used to normalize each sample and select highly variable genes. To further ensure that clustering would not be influenced by batch effects associated with mouse conditions, we performed the data integration method implemented by Seurat for *SCTransform*-normalized data. Especially, the *Prep-SCTIntegration* function was run to identify anchors, and the normalization method parameter was set to the value SCT when running *FindIntegrationAnchors* and *IntegrateData*, to obtain integrated data including six samples.

The integrated gene-barcode matrix was analyzed with PCA by using the top 3000 variable genes, and a shared nearest neighbor graph was constructed on the basis of the Euclidean distance in the low-dimensional subspace spanned by the selected significant principal components (dims = 1:40). Cells were clustered at an appropriate resolution (resolution = 0.1), then visualized with the two-dimensional uniform manifold approximation and projection for dimension reduction (UMAP) algorithm. DEG analysis for each cluster was performed with the Wilcoxon rank-sum test. Cell types were identified with various known markers. For different cell types, cells were grouped on the basis of known markers and analyzed with Seurat in a similar manner.

Differential gene expression and gene functional enrichment analysis

DEG analysis for each cell type was performed by the Wilcoxon rank-sum test with the Seurat function *FindAllMarkers*. We firstly filtered out the cell types that were either missing or accounted for fewer than 25% of the cells in the comparison groups. Differential expression analysis was performed to generate a set of differential genes ($|\log_2$ fold change$| > 0.25$, adjusted *P* value < 0.05). Visualization of markers was performed by violin plots or heatmap using the R packages MySeuratWrappers (v0.1.0) and pheatmap (v1.0.12).

For DEGs, gene ontology (GO) and Kyoto Encyclopedia of Genes and Genomes (KEGG) pathway analyses were performed with the R package clusterProfiler (v4.0.2) [33]. Multiple hypothesis testing correction was performed with the Benjamini–Hochberg procedure. Pathway analysis was performed by R package gene set variation analysis (GSVA) (v1.40.0) [34] with MSigDB Hallmark gene sets, and the differential gene sets were calculated with the R package limma (v3.48.1). Results with adjusted *P* value < 0.05 were further visualized with the R package ggplot2 (v3.3.5).

Transcription factor (TF) regulatory network analysis

TF regulons were identified with pySCENIC (v0.11.2) [35], a computational method to predict critical regulators and identify cell state from scRNA-seq data. The gene co-expression network was first generated with the gradient boosting machine via the *grn* function. Cis-regulatory motif analysis was performed with precomputed databases from cisTargetDB via the *ctx* function. The AUCell algorithm was used to score the activity of different regulons via the *aucell* function. To identify the cell-type specific regulons, we calculated the regulon specificity score (RSS) of each cell type via the function *regulon_specificity_scores* and visualized the results

Bai *et al. Military Medical Research*   (2023) 10:7

Page 5 of 22

with the R package pheatmap. Finally, the specific regulons including TF and target genes were imported into Cytoscape (v3.6.1) [36] for visualization.

Cell trajectory analysis

Cell trajectory analysis for hepatocytes, hepatic stellate cells (HSCs), B cells and macrophages was performed with the R package monocle (v2.20.0) [37]. DEGs in each subtype were input as variable genes. Then dimensionality reduction was applied to the data with the Reversed Graph Embedding algorithm. Finally, cell ordering was performed with manifold learning via the function *orderCells* and visualized via the function *plot_cell_trajectory*. Furthermore, branches that appeared in the trajectory were analyzed with branched expression analysis modeling (BEAM) to discover DEGs between branches via the function *BEAM* and were visualized via the function *plot_genes_branched_heatmap*.

RNA velocity-based estimation of cellular transition probability

RNA velocity analysis was performed with velocyto (v0.17) [38] with the default pipeline based on a steady-state model, and the future mRNA abundance of each gene from the ratio of spliced and unspliced mRNA levels was predicted and used as input data for scVelo (v0.2.4) [39]. This procedure enabled estimation of RNA velocity with a dynamic model to learn the full transcriptional dynamics of splicing kinetics. The unspliced/spliced phase trajectory was visualized via the function *velocity_embedding_stream* with UMAP coordinates of endothelial cells (Endos) from the Seurat package as the embedding coordinates for plotting.

Cell–cell communication inference

Cellular communication analysis was performed with cellphonedb (v2.1.4) [40], on the basis of the ligand-receptor interactions in different cell types. First, the R package biomaRt (v2.48.3) was used to transform gene names from mouse to human. Then the normalized genes expression matrix and cell type meta information served as the input for cellphonedb. The function *method statistical_analysis* was used to calculate the counts of ligand-receptor pairs of different cell types. The function *echartr* in the R package recharts (v0.2-1) was used to perform data visualization. We manually selected ligand-receptor pairs on the basis of *P* value < 0.05 and the mean expression of the average level in the present clusters.

Label-free proteomics measurement and data analysis

LX-2 and MIHA cells were treated with 10 μmol/L TCS for 24 h. The cells were then collected and the proteins were extracted with 8 mol/L urea in 1% sodium deoxycholate (SDC, w/v) buffer. Proteins were reduced and alkylated with DL-Dithiothreitol (DTT) and Iodoacetamide (IAA). After digesting with trypsin, the resulting peptides were desalted and subsequently analyzed in data-independent acquisition (DIA) mode with LC–MS/MS. The data were analyzed with DIA-NN software. The R package limma (v3.50.3) was used to identify significantly differentially expressed proteins (DEPs) with fold change ≥ 1.2 and adjusted *P* value < 0.05, and the results were visualized with volcano plots and heatmaps. The biological processes enrichment analysis of DEPs was performed with the GO database.

Metabolomic data analysis

LX-2 and MIHA cells were treated with TCS as described above, and the metabolites were then extracted and analyzed with LC–MS/MS. Raw files were input into Compound Discoverer 3.1 software to perform identification and quantification by matching with the mzCloud, mzVault and MassList databases. MetaboAnalyst 5.0 web server was used to perform the downstream analysis with default parameters. Significantly differentially expressed metabolites (DEMs) were identified on the basis of fold change ≥ 1.2 and *P* value < 0.05.

Statistical analysis

In non-scRNA-seq and mass spec data sets, data are presented as mean ± standard deviation unless stated otherwise by Graphpad Prism 8.0 (GraphPad Inc.). Schematic diagrams were created with BioRender.com. Two-tailed *t*-test was used to analyze the statistical differences between two groups and ordinary one-way analysis of variance (ANOVA) was used for multiple groups, unless otherwise mentioned. The differential tissue usages (in control and TCS group) were statistically significant based on a chi-square test to evaluate the cell proportion biases of subtypes for each sample [41]. *P* value < 0.05 was considered statistically significant.

Results

TCS induces hepatocyte hypertrophy in mice

We established a relatively short term TCS exposure mouse model to profile the early hepatotoxicity effects of TCS at the single cell level (Fig. 1a). After feeding with TCS for 14 d, the mice did not show any obvious signs of severe toxicity, as indicated by constant body weight (Fig. 1b). In addition, most of the blood or serum biomarkers in the panel were not affected, although some groups showed statistically significant changes with a small effective size (Additional file 1: Fig. S1a, b). The H&E staining on liver tissue showed mild histological changes after TCS exposure (Additional file 1: Fig. S1c). Moreover, the relative liver weights increased in the
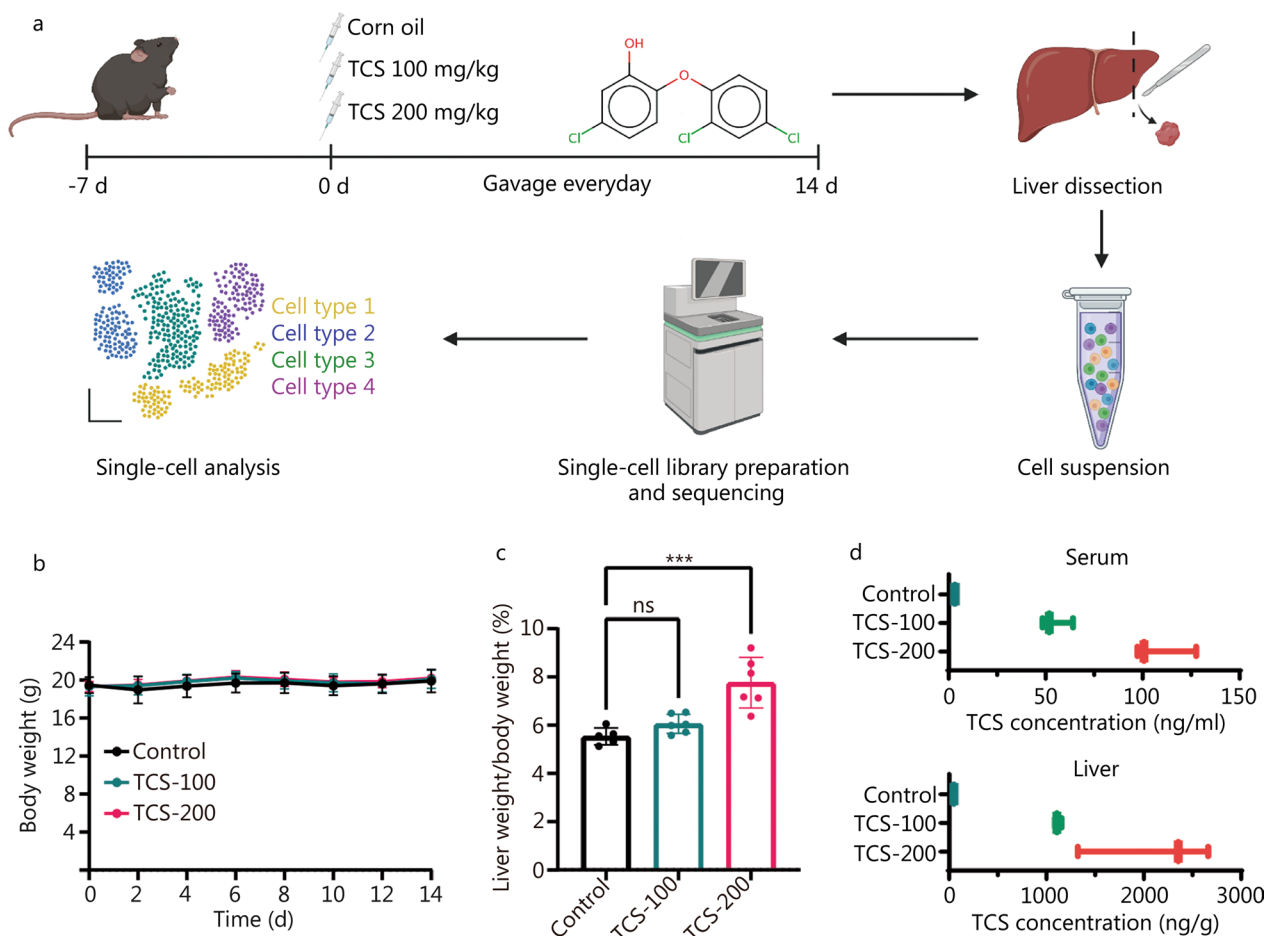
Fig. 1 TCS induced hepatocyte hypertrophy in mice liver. **a** Experimental scheme and workflow diagram. **b** Body weight of mice in different groups. **c** The liver/body weight ratio in different groups ($n=6$). **d** The TCS concentrations in mice serum and liver tissues after 14 d treatment ($n=3$). TCS triclosan, ns non-significant, ***$P<0.001$

treatment group, and the difference became statistically significant in mice exposed to 200 mg/kg of TCS ($P<0.001$, Fig. 1c), in agreement with previous reports [23, 24]. In contrast, the weights of other organs such as the spleen and kidneys were not affected ($P>0.05$, Additional file 1: Fig. S1d). We then determined the TCS concentrations in the serum and liver tissue with LC–MS/MS (Additional file 1: Fig. S2). The serum concentrations of free TCS were 54.8 ng/ml (0.19 μmol/L) and 108.56 ng/ml (0.37 μmol/L) after exposure to 100 mg/kg and 200 mg/kg of TCS, respectively (Fig. 1d). The concentrations of TCS in the liver were much higher, reaching 1117.51 ng/g and 2112.73 ng/g, respectively (Fig. 1d), suggesting that the liver is the main organ of accumulation and metabolism of TCS in the body [42]. In summary, 14 d of TCS exposure caused obvious hepatocyte hypertrophy at a dose of 200 mg/(kg·d). This group was then chosen for further single-cell analysis to better understand the underlying mechanism.

Single-cell transcriptome profiling identifies different cell types

We then investigated the cellular and molecular mechanisms of TCS by carrying out a single cell transcriptional profiling of liver tissues from three control and three TCS-treated (group of 200 mg/kg) mice by using 10× Genomics technology. A total of 76,209 cells (37,841 for control group and 38,368 for TCS-200 group) were retained for further analysis, after data quality control at the gene and cell levels (details in Methods, Additional file 1: Fig. S3). We identified 13 major cell types (Fig. 2a) according to the expression of canonical markers in mouse liver (Fig. 2b, c), including B cells ($n=10,642$, expressing *Cd79a*, *Cd79b* and *Ms4a1*), Basophils ($n=227$, expressing *Cap3*, *Ms4a2* and *Mcpt8*), Cholangiocytes ($n=351$, expressing *Epcam*, *Sox9* and *Krt19*), Endos ($n=30,750$, expressing *Pecam1*, *Clec4g* and *Kdr*), Erythrocytes ($n=1615$, expressing *Hba-a1* and *Hba-a2*), hepatocytes (Heps, $n=11,011$, expressing *Alb*
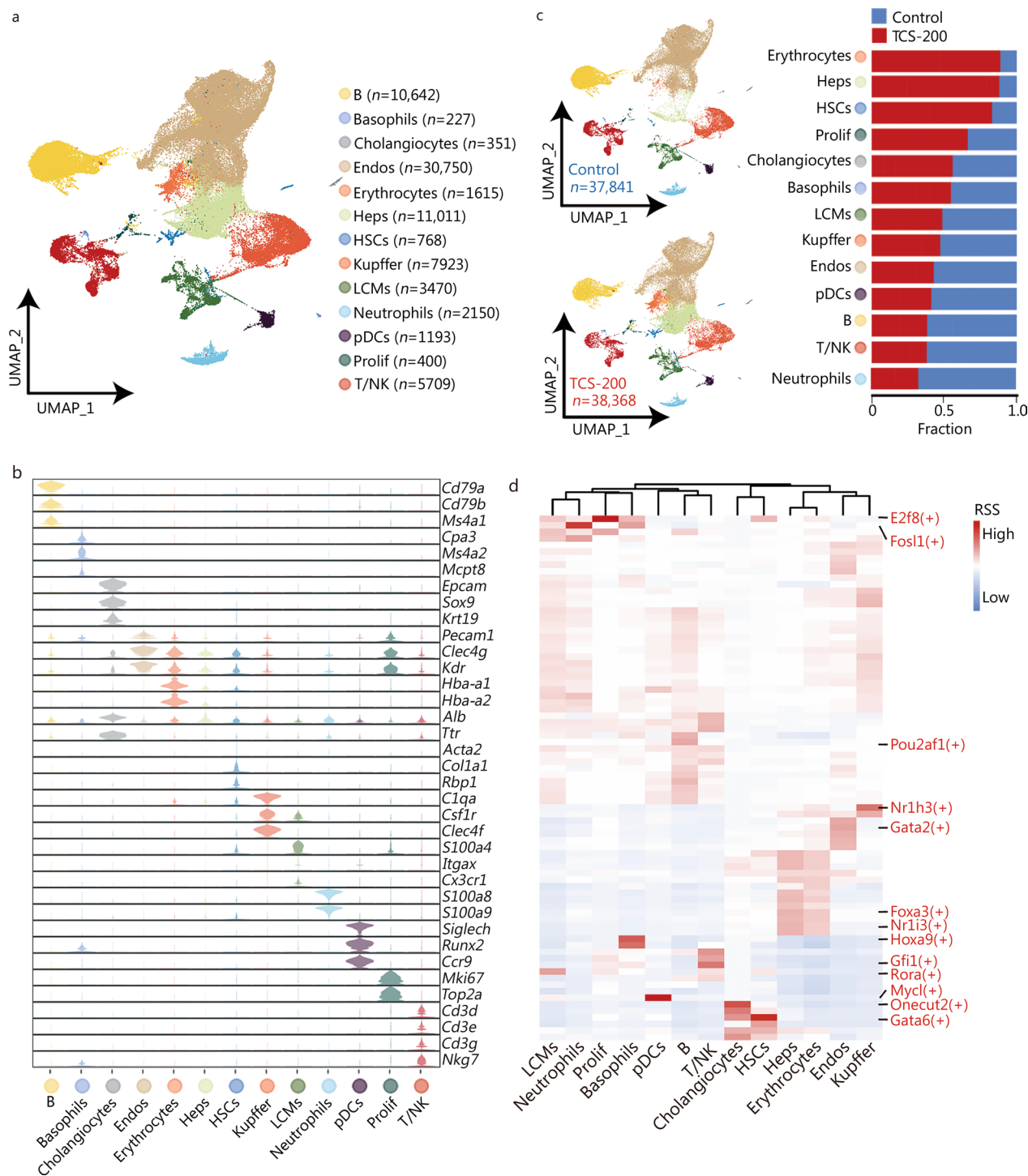
Fig. 2 Cell diversity in mice liver cells delineated by single-cell transcriptome. **a** UMAP visualization of 13 cell types based on 76,209 single-cell transcriptomes. Cell counts for each individual cell type are indicated in parentheses. Each dot represents a single cell. **b** Violin plots showing the expression levels of representative markers in each cell type. **c** Distribution of each cell type in control and TCS-200 groups. The bar chart showed the relative fraction of each cell type in different groups. **d** Heatmap of transcription factor (TF) activities in each cell type. UMAP Uniform Manifold Approximation and Projection for Dimension Reduction, Endos endothelial cells, Heps hepatocytes, HSCs hepatic stellate cells, LCMs liver capsular macrophages, pDCs plasmacytoid dendritic cells, Prolif proliferative cells, T/NK T/natural killer cells, TCS triclosan, RSS regulon specificity score

Bai *et al. Military Medical Research*   (2023) 10:7

Page 8 of 22

and *Ttr*), HSCs ($n = 768$, expressing *Acta2*, *Col1a1* and *Rbp1*), Kupffer cells ($n = 7923$, expressing *C1qa*, *Csf1r* and *Clec4f*), liver capsular macrophages (LCMs, $n = 3470$, expressing *S100a4*, *Itgax* and *Cx3cr1*), Neutrophils ($n = 2150$, expressing *S100a8* and *S100a9*), plasmacytoid dendritic cells (pDCs, $n = 1193$, expressing *Siglech*, *Runx2* and *Ccr9*), proliferative cells (Prolif, $n = 400$, expressing *Mki67* and *Top2a*) and T/natural killer (NK) cells ($n = 5709$, expressing *Cd3d*, *Cd3e*, *Cd3g* and *Nkg7*). The top 10 DEGs of each cell type are shown in Additional file 1: Fig. S4.

To support our cell type identification, we applied single-cell regulatory network inference and clustering to all cells and identified the TFs with the highest RSS in each cell type (Fig. 2d). For instance, E2f8 (an important modulator of the cell cycle that induce cell proliferation) in Prolif cells, Pou2af1 (a lymphocyte transcriptional coactivator expressed mainly in B cells associated with the formation of germinal centers) in B cells, and Nr1i3 (a constitutive androstane receptor that promotes proliferation of liver cells) in Heps. Among these cell types, the proportion of Heps was higher in the TCS-200 than control group, in agreement with our observation of greater liver weight. In addition, the HSCs, Erythrocytes and Prolif cells also showed higher proportions in TCS-200 group than control group (Fig. 2c). We then comprehensively analyzed how TCS affects specific cell (sub)types in exerting its hepatotoxicity effects.

Heps exhibit proliferation- and fibrosis-associated characteristics after TCS treatment

As described above, the number of Heps significantly increased after TCS treatment (Fig. 2c). To explore how TCS alters Heps, we analyzed the DEGs in the transcriptomes of control and TCS (200 mg/kg)-treated Heps (Additional file 1: Fig. S5a). Compared with those in control group, Heps in TCS-200 group exhibited greater expression of genes involved in extracellular matrix (ECM) structural constituent, ECM organization, collagen-containing ECM, and regulation of epithelial cell proliferation (Fig. 3a). In contrast, the expression of genes involved in fatty acid metabolic process, tryptophan metabolism and drug metabolism were significantly down-regulated, thereby indicating the possible impairment of the metabolic functions of Heps, as further confirmed by metabolomics analysis (Fig. 3a; Additional file 1: Fig. S5b, c). The GSVA analysis results indicated that pathways associated with Notch signaling, epithelial-mesenchymal transition (EMT) and Hedgehog signaling (Additional file 1: Fig. S5d), which are associated with liver regeneration and fibrosis, were also activated in TCS-200 group.

Next, Heps were divided into four subtypes at a higher resolution, which were termed Hep1, Hep2, Hep3 and Hep4, respectively (Fig. 3b). Cells from control group clustered mainly in Hep1, whereas cells in TCS-200 group clustered mainly in Hep2 and Hep3. Clustering analysis of these subtypes revealed unique transcriptomic signatures. Functional enrichment analysis suggested the involvement of Hep1 in retinol and fatty acid metabolism, and the involvement of Hep3 in collagen trimer formation and binding (Additional file 1: Fig. S5e). Interestingly, Hep2 cells were involved in both retinol metabolism and collagen related processes, thus suggesting a mixed or transitional state of Hep1 and Hep3 subtypes. Furthermore, the drug metabolism-associated signatures were enriched in Hep1 cells, ECM- and EMT-associated genes were enriched in Hep2 and Hep3 cells, and cell proliferation signals were intensely enriched in Hep3 cells (Fig. 3c).

To understand the transcriptional dynamics of Heps during TCS treatment, we reconstructed cell–cell relationships through pseudotime trajectory analysis (Fig. 3d). The results suggested that the trajectory began with Hep1 cells, and most Hep2 cells progressed to the Hep3 phenotype, in agreement with the UMAP location and pathway enrichment analysis (Fig. 3b, Additional file 1: Fig. S5e).

In addition, we used pySCENIC to map the gene regulatory networks governing these subtypes. Marked differences in the regulon activity were observed among different treatment and cell subtypes, thus again supporting that distinct cell states were induced by TCS (Fig. 3e). The Hep2 and Hep3 cells in TCS-200 group had elevated regulon activity for Gata2 and Mef2c (Additional file 1: Fig. S5f), which are known to be associated with development and oncogenesis [43, 44]. The up-regulation of the protein expression levels of GATA2 and MEF2C was also confirmed through both in vivo and in vitro treatment experiments (Fig. 3f, g; Additional file 1: Fig. S5g). Target genes regulated by Gata2 and Mef2c are enriched in processes associated with the response to transforming growth factor beta (*Tgfb2*, *Eng* and *Bmp2*), EMT (*Tgfb2*, *Bmp2*, *Eng* and *Gja1*) and ECM organization (*Timp3*, *Sparc*, *Tgfb2*, *Ramp2*, *Adamts1*, *Serpinh1*, *Eng* and *Bmp2*) and collagen fiber assembly (*Bgn*) (Additional file 1: Fig. S5h). Moreover, Jun, an important TF regulating a large number of genes, was up-regulated by TCS treatment. Jun promotes hepatocyte survival and the progression from steatosis to NASH, whereas the expression of Jun in non-parenchymal liver cells is known to correlate with fibrosis [45].

We also performed quantitative proteomics analysis of DEPs after TCS treatment of the MIHA normal human
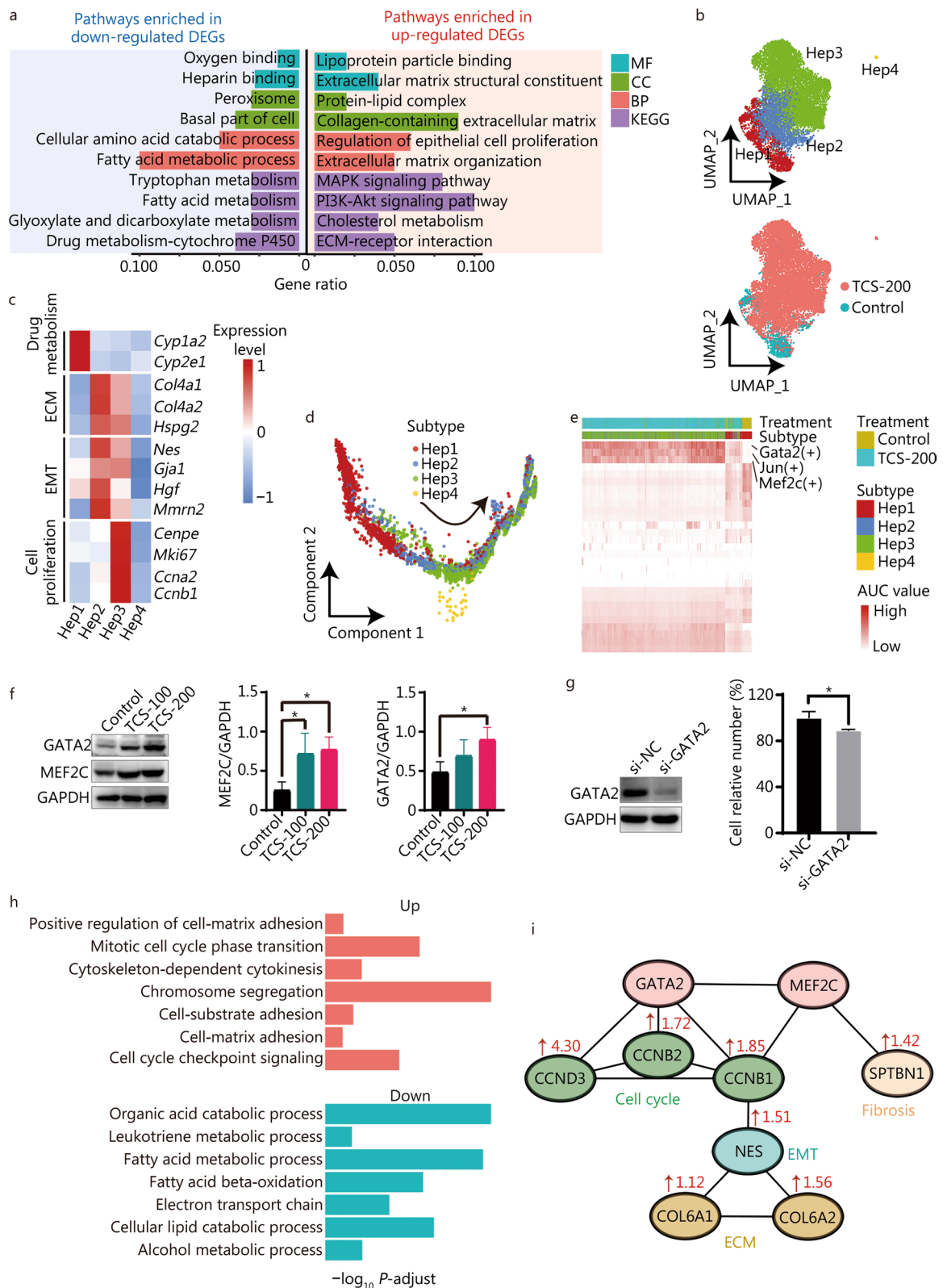
Fig. 3 (See legend on next page.)

Fig. 3 Heterogeneity of hepatocytes (Heps) and their differentiation states. **a** Functional enrichment in the down-regulated (left) and up-regulated (right) DEGs of TCS-200 group vs. control group. **b** UMAP visualization of distinct subtypes of Heps and their distributions in different groups. **c** Heatmap of expression levels of representative markers involved in drug metabolism, ECM, EMT and cell proliferation. **d** Pseudotime trajectory indicating the development of four subtypes, rooting from Hep1. **e** Heatmap showing AUC values of the expression levels of TFs in different subtypes. **f** The protein level of GATA2 and MEF2C in mice liver were detected by Western blotting. **g** Cell viability measured by CCK-8 assay after 72 h after transfection with si-NC for NC (normal control) or si-GATA2. **h** Bar plots showing the biological processes enrich up- and down-regulated DEPs after TCS treatment. **i** The potential regulatory relationship of GATA2 and MEF2C controlled downstream proteins leading to cell proliferation, ECM reorganization and liver fibrosis. Numbers indicate the fold change of protein between TCS-200 and control groups from proteomics dataset. TCS triclosan, DEGs differentially expressed genes, ECM extracellular matrix, MF molecular function, CC cellular component, BP biological process, KEGG Kyoto Encyclopedia of Genes and Genomes, AUC area under the curve, TF transcription factor, UMAP uniform manifold approximation and projection for dimension reduction, EMT epithelial-mesenchymal transition

hepatocyte cell line (Additional file 1: Fig. S5i). The up-regulated DEPs were enriched mainly in cell–matrix adhesion and the cell cycle, whereas the down-regulated DEPs were enriched in metabolic processes (Fig. 3h). We examined the measured changes in expression of the proteins regulated by *Gata2* and *Mef2c*, including those associated with drug metabolism (CYP4F12, CYP27A1 and CYP4F11), cell cycle (CENPF, CCND3, CCNB1 and CCNB2) and collagen formation (COL6A1, COL6A2 and NES), all of which showed trends consistent with the scRNA-seq results (Additional file 1: Fig. S5j). Thus, we next used the Search Tool for the Retrieval of INteracting Genes/proteins (STRING) database to construct a protein–protein interaction network for these proteins, to better understand the regulatory relationships among these key DEPs (Fig. 3i). GATA2 plays an important role in controlling the expression of cell cycle associated proteins (such as CCNB1, CCNB2 and CCND3). GATA2 and MEF2C up-regulate the expression of CCNB1 and NES (involved in EMT), thereby up-regulating the collagen proteins COL6A1 and COL6A2. Furthermore, MEF2C directly activates SPTBN1 and consequently induces liver fibrosis [46].

In summary, these findings indicated that TCS induces the proliferation of normal Heps, down-regulates retinol and fatty acid metabolism, and promotes fibrogenesis by accelerating ECM-associated processes, in which Gata2 and Mef2c are the key driving TFs.

HSCs are activated after TCS treatment

HSCs, one of the key non-parenchymal cell types in the liver, serve as the major origin of ECM proteins after injury. Beyond the increase in HSCs in TCS-200 group (Fig. 2c), GO analysis indicated that TCS induced the down-regulation of genes involved in lipid oxidation and storage, and the up-regulation of genes involved in collagen biosynthetic process, macrophage chemotaxis and the cell cycle (Additional file 1: Fig. S6a).

HSCs were divided into one quiescent subtype (qHSC) and seven activated subtypes (aHSC1–6 and

aHSC_prof), among which aHSC_prof exhibited cell proliferation features, at a higher resolution (Fig. 4a). Among these subtypes, qHSC accounted for the highest proportion in control sample (32.3%, $n = 42$ of 130) but only 7.2% ($n = 46$ of 638) in the TCS treatment sample (Additional file 1: Fig. S6b). Notably, aHSC1 and aHSC2 showed overexpression of genes involved in ECM remodeling and fibrosis, thus suggesting roles in the development of liver fibrosis. In addition, aHSC4 was enriched in the expression of chemotactic cytokines including *Ccl6*, *Cxcl10*, *Ccl24* and *Ccr2* (Fig. 4b).

Similarly, pseudotime analysis was performed to follow the transcriptomic changes in HSCs after TCS treatment. The results indicated that qHSC developed into primarily aHSC1 (referred to as cell fate 1) or aHSC4 (referred to as cell fate 2) (Fig. 4c), accompanied by aHSC2, aHSC_prof and so on. To further explore the molecular events underlying the different trajectories, we used BEAM to analyze the branch-dependent DEGs (Additional file 1: Fig. S6c). Cell fate 2, the lineage from qHSC to aHSC4, showed the overexpression of genes involved in chemotaxis such as *Ccl6*, *Cxcl2*, *Cxcl13*, *Ccl3*, *Ccr2* and *Ccr12*, in agreement with the subtype cell markers shown in Fig. 4b. In contrast, cell fate 1, the lineage from qHSC to aHSC1, was enriched in the expression of genes involved in ECM organization and collagen fibril organization.

Because the activation of HSCs is known to be the key driver of liver fibrogenesis, and our analysis indicated that TCS induced the proliferation and activation of HSCs, we performed Masson's trichrome and Sirius red staining and western blotting to validate the progression of fibrogenesis. TCS was found to increase collagen deposition in mouse liver and to have a statistically significant effect in the 200 mg/kg dosage group (Fig. 4d). In addition, the protein expression level of α-SMA (an important marker of fibrogenesis) (Fig. 4e) and the hepatic deposition level of collagen I were elevated, as expected (Fig. 4f). We also validated that TCS promoted the expression of α-SMA and collagen I in LX-2, a human HSC line (Fig. 4g, h).
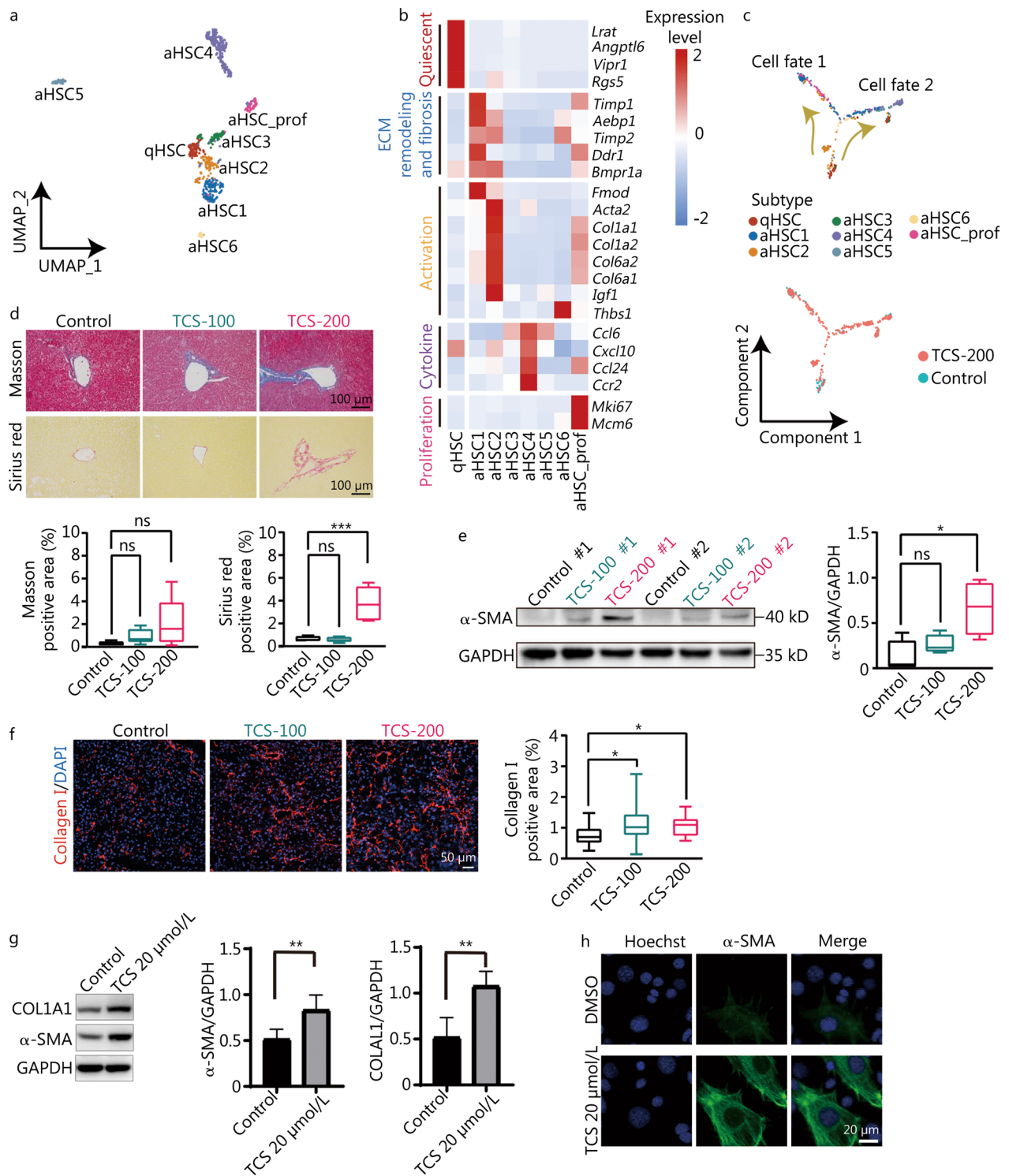
Fig. 4 (See legend on next page.)

Bai *et al. Military Medical Research* (2023) 10:7

Page 12 of 22

(See figure on previous page.)

Fig. 4 Transcriptomic roadmap of HSCs activation. **a** UMAP visualization of eight distinct subtypes of HSCs. **b** Heatmap of expression levels of representative markers related to cell quiescence, ECM remodeling and fibrosis, activation, cytokine and proliferation. **c** Pseudotime trajectory indicating the development of HSCs subtypes. Cell fate 1 represents trajectory from qHSC to aHSC1, cell fate 2 represents from qHSC to aHSC4. **d** Masson and Sirius red staining and the corresponding quantification of Masson- and Sirius red-positive areas ($n = 5$). Scale bar $= 1000$ μm. **e** Western blotting analysis of α-SMA expression levels in mice liver with or without TCS treatment, and the corresponding quantification of α-SMA protein expression levels, relative to GADPH loading control ($n = 4$). **f** Immunofluorescence staining of collagen I on mouse liver frozen sections ($n = 4$). The collagen I positive area was analyzed by ImageJ. Scale bar $= 50$ μm. **g** The protein expression of COL1A1 and α-SMA in LX-2 cells after TCS treatment. **h** Immunofluorescence staining of α-SMA in LX-2 cells after TCS or DMSO treatment. Scale bar $= 20$ μm. HSCs hepatic stellate cells, UMAP uniform manifold approximation and projection for dimension reduction, qHSC quiescent hepatic stellate cells, aHSC activated hepatic stellate cells, ECM extracellular matrix, TCS triclosan, α-SMA alpha smooth muscle actin, ns non-significant; *$P < 0.05$, **$P < 0.01$

In the proteomics analysis performed on LX-2 cells, up-regulated DEPs were mostly associated with cell cycle transition, whereas down-regulated DEPs were enriched in RNA localization, regulation of glycogen biosynthetic process and oxidative phosphorylation (Additional file 1: Fig. S6d, e), in good agreement with the scRNA-seq results (Additional file 1: Fig. S6a). Notably, proteins associated with collagen organization (COL6A2, COL4A2, COL6A1, COL16A1 and BMP1) and the cell cycle (UBE2E2, TOP2A and CDK14) were elevated in TCS-200 group (Additional file 1: Fig. S6f), thus further supporting the proliferation and activation characterization of HSCs after TCS treatment.

These results revealed that TCS treatment drives the development of HSCs from quiescent cells into several different activated phenotypes, particularly the aHSC1 subtype, which showed overexpression of ECM genes (directly associated with fibrosis), and the aHSC4 subtype, which showed overexpression of chemotactic chemokines (associated with cell migration).

Endos undergo dysfunction and capillarization after TCS treatment

Liver Endos, including sinusoidal endothelial cells (LSECs) and vascular endothelial cells (LVECs), as well as lymphatic endothelial cells, are the largest group of cells within the non-parenchymal cells of the liver, and they regulate liver homeostasis and intrahepatic vascular tone [47]. The genes up-regulated after TCS treatment among Endos, with respect to the expression in control group, were found to be involved in cellular response to external stimulus, the canonical Wnt signaling pathway, response to hypoxia and fibroblast proliferation (Additional file 1: Fig. S7), whereas the down-regulated genes were involved in the regulation of vasculature development, endothelial cell proliferation and chemotaxis.

According to the spatial lobular locations, we divided Endos into two LVEC subtypes and five LSEC subtypes (Fig. 5a), which were mapped on the liver lobule from the portal tract to the central venous regions according to the expression levels of portal, periportal, middle, pericentral and central markers (Fig. 5b). Notably, the proportion of the LSEC_mid2 subtype exhibited the most significant increase after TCS treatment, and contained more DEGs than control group (Fig. 5c, d). The functional enrichment of the up-regulated genes in this subtype suggested their participation in liver development, collagen trimer assembly, ECM binding, PPAR signaling pathway and TGF-β signaling pathway (Fig. 5d), which are associated with the promotion of liver fibrosis. We then examined TCS-induced physiological functional changes in Endos. Endos remove circulating antigens and toxins via different endocytic receptors [48], including Mrc1, Stab1 and Stab2, all of which significantly decreased after TCS treatment (Fig. 5e). Moreover, Endos respond to increased shear stress to maintain normal vascular through the activation of TFs such as Klf2, Fos and Junb, which were markedly suppressed, thus suggesting TCS-induced dysfunction of Endos.

At the onset of liver fibrosis, LSECs undergo capillarization (loss of fenestrae) and produce basement membrane—a phenotype mimicking that of common LVECs [47–49]. To explore whether this phenotypic change also existed in our model, we performed RNA velocity analysis to estimate the cellular transition probability and indeed found a tendency for most LSEC_pc and some LSEC_mid2 cells to transform into LVEC_central cells (Fig. 5f). Furthermore, we constructed gene regulatory networks for the seven subtypes and found that Hlf exhibited the highest RSS in LSEC_mid2 cells (Fig. 5g). The target genes regulated by Hlf were mainly involved in liver development (*Proc*, *Abcb11*, *Prox1*, *Egfr* and *Hp*), extracellular structure organization (*Gas2*, *Itih1*, *Jup* and *Nr1h4*), tissue remodeling (*Ahsg* and *Egfr*) and response to hypoxia (*Ang*, *Acaa2*, *Hp* and *Egfr*) (Fig. 5h).

Overall, these results indicated TCS-induced dysfunction of Endos, showing diminished endocytic and vascular developmental/regulatory ability, whereas the ECM-associated processes and collagen trimer assembly were up-regulated. In addition, the phenotypic shift of most LSEC_pc and some LSEC_mid2 toward LVEC_central cells (i.e., capillarization), indicating the occurrence
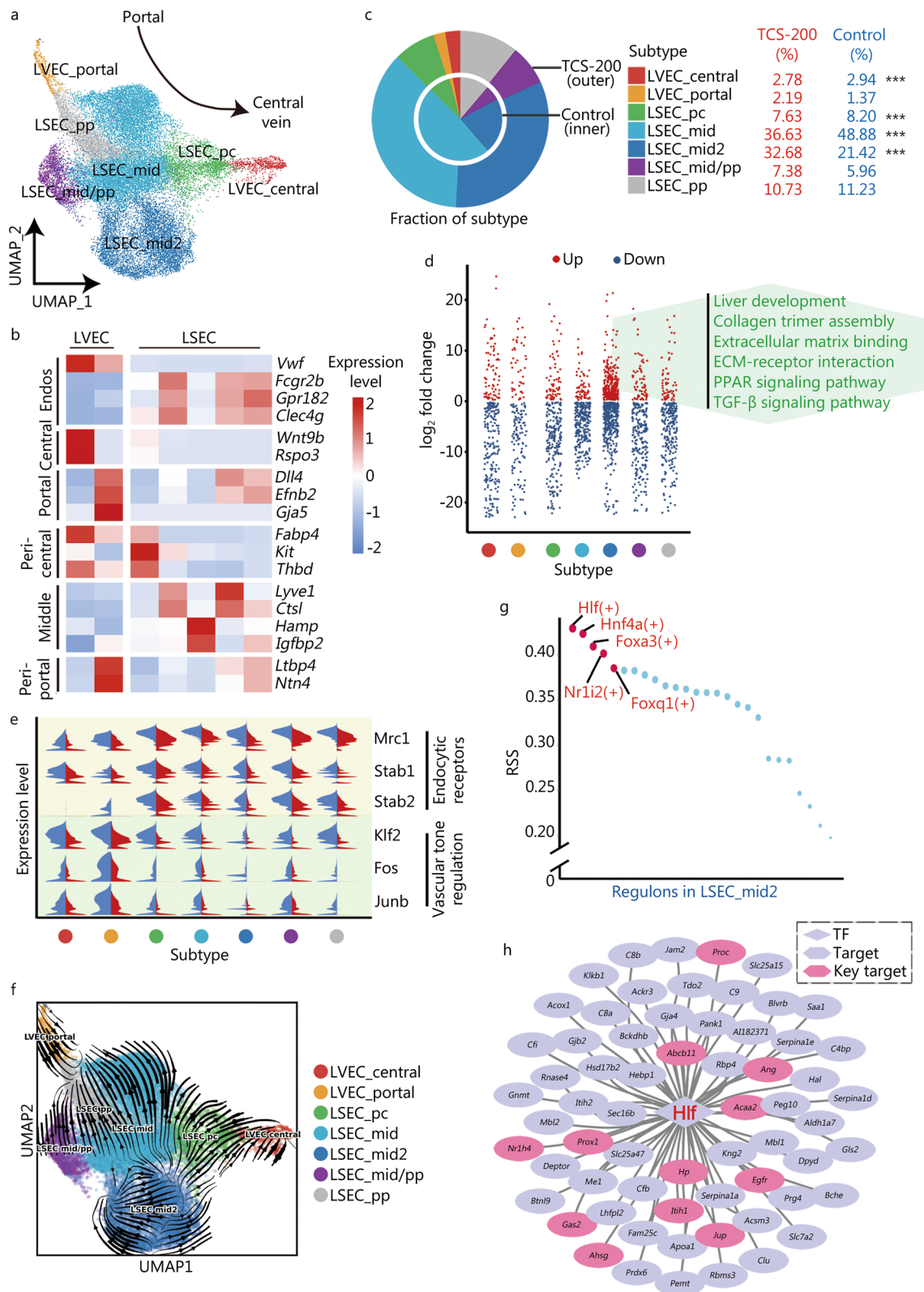
Fig. 5 (See legend on next page.)

(See figure on previous page.)

Fig. 5 Distinct endothelial cells according to the spatial locations. **a** UMAP visualization of the 7 distinct subtypes of Endos based on spatial distribution. **b** Heatmap of the expression levels of representative markers indicating generalized Endos as well as central, pericentral, middle, periportal and portal position. **c** Pie chart showing the fraction of each endothelial subtype. **d** Strip chart showing DEGs of each subtype after TCS-200 treatment. The texts in green color represents the pathways enriched in the up-regulated DEGs in LSEC_mid2. **e** Split violin plot of the expression levels of genes associated with endocytic receptors and vascular tone regulation. **f** RNA velocity analysis of different subtypes of Endos, indicating LSEC capillarization. **g** Scatter diagram showing RSS of TFs in LSEC_mid2 subtype. The top 5 TFs ordered by scores were listed. **h** Transcription regulatory network constructed by Hlf and its target genes. Red text represents TFs, black text for targets (target), pink hexagon for genes related to ECM, tissue remodeling and response to hypoxia (key target). Endos endothelial cells, LVEC liver vascular endothelial cells, LSEC liver sinusoidal endothelial cells, UMAP uniform manifold approximation and projection for dimension reduction, DEGs differentially expressed genes, TCS triclosan, ECM extracellular matrix, RSS regulon specificity score, TFs transcription factors; ***$P < 0.001$

of liver fibrosis, appeared to be under the control of Hlf activation.

B plasma cells with fibrotic characteristics increase after TCS treatment

Lymphocytes, including T, NK and B cells, play important roles in the pathogenesis of liver disease. We next analyzed how TCS affects lymphocytes in mouse livers. First, we identified the subtypes of lymphocytes according to the expression of key marker proteins. NK cells were divided into two subtypes: NK_cyto (expressing *Prf1*) and NK_inflam (expressing *Xcl1*), which have cytotoxic and inflammatory characteristics, respectively (Fig. 6a, b). Similarly, T cells contained naive (expressing *Lef1*, *Ccr7* and *Tcf7*), effector (expressing *Fasl*, *Ifng* and *Gzmk*), memory (expressing *Cxcr3*, *Cxcr6* and *Cd40lg*) and regulatory (expressing *Foxp3* and *Ctla4*) subtypes, and NKT cells were characterized by both T and NK cell signatures. Three subtypes of B cells were identified: naive (expressing *Ighd*, *Fcmr*), memory (expressing *Cd38*) and plasma (acting as effector B cells with overexpression of *Igha* and *Jchain*) cells. Notably, B_plasma showed the most significant increase (up to 23-fold) after TCS-200 treatment (11.95% vs. 0.51%) (Fig. 6c), thus supporting the requirement of B cells for liver fibrogenesis [50].

Consequently, we reconstructed the developmental trajectory of B cells (Fig. 6d) and found that B_naive cells differentiated into B_plasma or B_memory subtypes, the latter of which was also accompanied by a minor population of B_plasma cells. To further explore the molecular mechanisms underlying the different trajectories, we retrieved the branch-dependent DEGs and performed biological processes enrichment analysis (Fig. 6e). The results suggested that B_naive cells (State 3) were enriched in genes involved in B cell activation and differentiation; B_memory cells (cell fate 1, State 4) were enriched in genes involved in tissue migration and the cell cycle transition; and B_plasma cells (cell fate 2, State 5) were enriched in genes involved in acute-phase response, collagen-containing ECM and hepatocyte

proliferation. Furthermore, DEGs of B_plasma cells after TCS treatment (up = 497, down = 74) were identified (Fig. 6f). The up-regulated genes were enriched in ECM organization, response to hypoxia, tissue remodeling and fibroblast proliferation (Fig. 6g), many of which are associated with liver fibrogenesis.

These results revealed that the TCS-induced increase in B plasma cells might be the key subtype of lymphocytes contributing to the progression of liver fibrosis.

LCMs and Kupffer cells display M2-skewed phenotype after TCS treatment

Myeloid cells, consisting of granulocytes, monocytes, macrophages, dendritic cells and so on, show heterogeneous distributions and self-replenish in response to drug-induced injury in the liver [51]. LCMs and Kupffer cells can be further divided into M1 (expressing *Cd86* and *Cd68*), M2 (expressing *Tgfb2*, *Wnt5a* and *Mrc1*) and proliferation (expressing *Mki67*, *Stmn1*, *Cenpf* and *Ccnb2*) subtypes (Additional file 1: Fig. S8a, b). Among them, the proportions of the M2 and proliferation subtypes increased after TCS treatment (Additional file 1: Fig. S8c). Interestingly, the pseudotime trajectory analysis also suggested differentiation of the M1 subtype of LCM and Kupffer cells into the M2 subtype, along with the distribution of the proliferation cells (Additional file 1: Fig. S8d), thus resulting in M2-skewed polarization. Previous study has demonstrated that macrophages in the fibrotic liver exhibit M2-preponderant activation [52], thereby further supporting TCS treatment-induced liver fibrosis.

Moreover, after TCS treatment, 376 (up = 239, down = 137) and 1118 (up = 703, down = 415) DEGs were identified in the LCM_M2 and KC_M2 subtypes, respectively (Additional file 1: Fig. S8e), including the upregulation of several pro-fibrosis genes, such as *Ccl2* and *Il1b* in LCM_M2, *Il6* and *Mmp2* in KC_M2, as well as *Apom* and *Spp1* in both LCM_M2 and KC_M2. In addition, genes associated with ECM (*Fbn1*, *Col14a1*, *Ecm1*, *Mgp* and *Col1a1*), ECM fibrosis (*Pdgfra* and *Lrp1*), ECM remodeling (*Adamts5*) and proteoglycan assembly (*Lum*) were up-regulated in KC_M2 cells. Finally, we performed
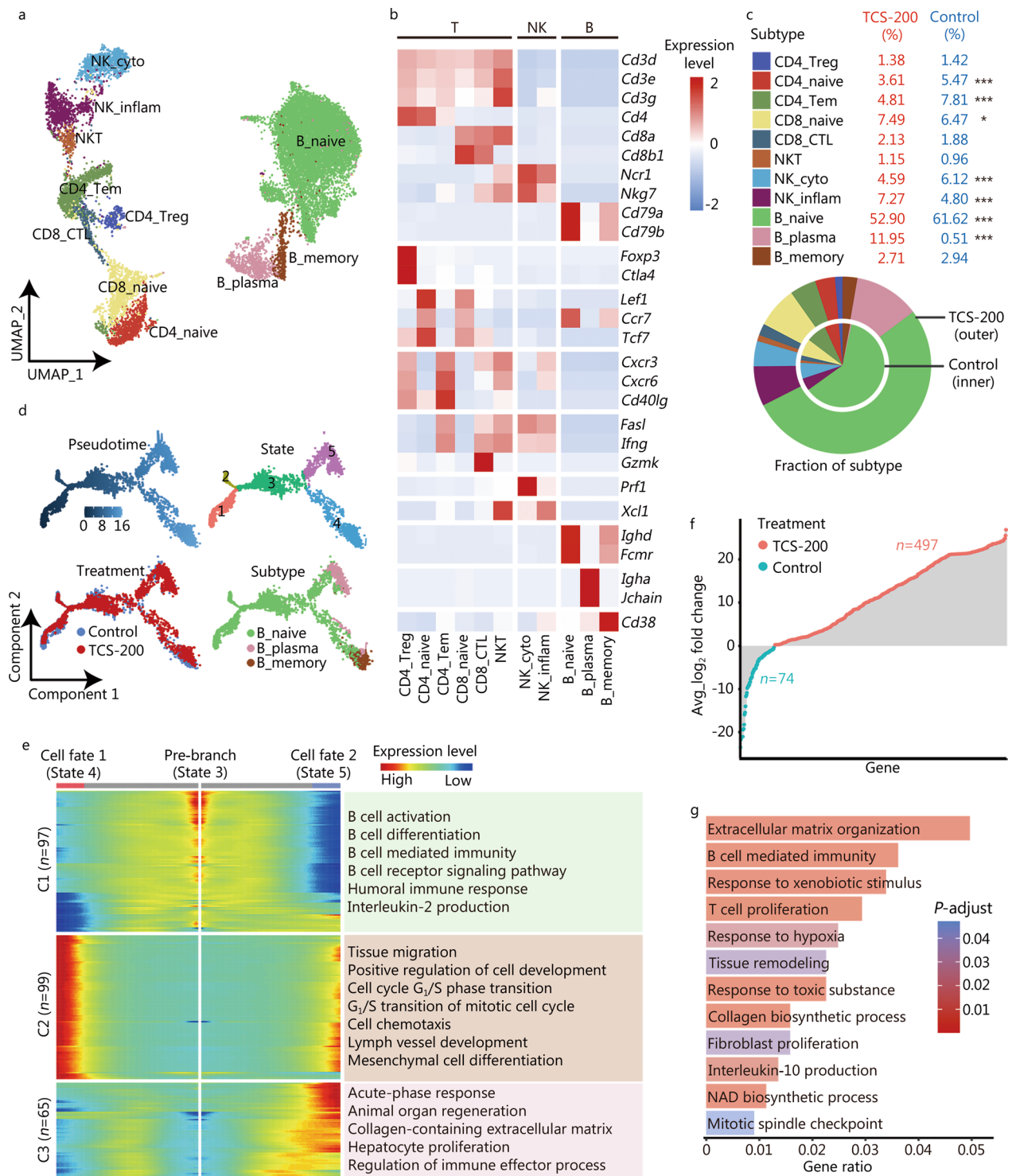
Fig. 6 (See legend on next page.)

(See figure on previous page.)

Fig. 6 Dynamic regulation of lymphocytes after TCS treatment. **a** UMAP visualization of distinct subtypes of lymphocytes including B, T and NK cells. **b** Heatmap of the expression levels of representative markers indicating lymphocytes, regulatory, naive, memory, effector, cytotoxic, and inflammatory functions. **c** Pie chart showing the relative fraction of each lymphocyte subtype. **d** Pseudotime trajectory indicating the development of B cell subtypes. The different color schemes represent the segregation based on pseudotime, cell state, treatment and subtype, respectively. **e** BEAM showing genes involved in the differential development of cell fate 1 (State 4) and cell fate 2 (State 5), and the enriched GO terms were listed at right. **f** Lollipop chart depicting the DEGs of B plasma cells after the TCS-200 treatment. Red represents up-regulated and blue represents down-regulated genes. **g** Bar graph showing the functions enriched in up-regulated DEGs of B plasma cells after the TCS-200 treatment. Length represents gene ratio and color represents adjusted *P* value. UMAP uniform manifold approximation and projection for dimension reduction, NK natural killer cells, C1 cluster 1, C2 cluster 2, C3 cluster 3, BEAM branched expression analysis modeling, GO Gene Ontology, DEGs differentially expressed genes, TCS triclosan; $*P < 0.05$, $***P < 0.001$

functional enrichment analysis of the up-regulated DEGs of KC_M2 (Additional file 1: Fig. S8f), which indicated enrichment in biological progresses involved in collagen ECM organization, fibroblast proliferation, macrophage chemotaxis, response to hypoxia and T-helper (Th)2 cell cytokine production. Of note, the excessive secretion of Th2 cytokine has been reported to be associated with excessive activation of M2 macrophages and to be positively correlated with the severity of fibrosis [53].

In summary, these results suggested the skewing of macrophages from M1 to M2 phenotype, and the discovery of several key genes likely to contribute to the progression of liver fibrosis.

Cell–cell communication crosstalk within the crucial subtypes

To explore differential cell–cell interactions after TCS treatment, we constructed a cellular communication network among different cell types with potential ligand-receptor pairs (Additional file 1: Fig. S9a). We observed relatively more counts of interactions in HSCs, Kupffer, LCMs and Endos cells acting either as source or target cells. We confirmed the enhanced interactions between macrophages and HSCs, and between macrophages and LSECs, in the TCS treatment group (Additional file 1: Fig. S9b). Given the analytic results for individual cell types, we focused on the cellular communication among the Hep2, Hep3, aHSC1, LSEC_mid2, B_plasma, KC_M2 and LCM_M2 subtypes (Additional file 1: Fig. S9c), all of which showed potential associations with the progression of liver fibrosis after TCS treatment. The interaction counts were particularly high in aHSC1, KC_M2 and LSEC_mid2 cells.

The key ligand-receptor pairs forming the interaction network are summarized in Fig. 7a. Many of the ligand-receptor pairs have been reported to be involved in fibrosis, such as IL6 receptor_IL6, TGFB2/3_TGF-beta receptor2/3, NOTCH1_WNT4, MERTK_GAS6 and TNF_TNFRSF1A [54–57]. As shown in Additional file 1: Fig. S9c, aHSC1 exhibited ligand-receptor pairs interacting with the other subtypes. For the ligands on aHSC1 cells, the most significantly enriched pairs comprised

collagen molecule and the corresponding complex on all subtypes, in line with excessive ECM formation when HSCs are activated. We confirmed that the protein levels of collagen I and ITGB1 (one subunit of a1b1 complex) were both elevated in TCS-treated mouse livers (Figs. 4f, 7b). Among these ligand-receptor pairs, we observed that GAS6 from LSECs and macrophages showed strong communication with aHSC1 through AXL. It was reported that GAS6_AXL pathway is associated with fibrosis [58], we further verified the involvement of the GAS6_AXL pathway in TCS-induced fibrosis. We first confirmed that the protein level of GAS6 was elevated in TCS-treated mouse liver (Fig. 7b). TCS also promoted the expression of α-SMA and phosphorylated Akt (p-Akt) (Fig. 7c). After incubation with recombinant GAS6 (rGAS6), HSC LX-2 cells also showed increased expression of α-SMA and p-Akt (Fig. 7d). Moreover, the AXL inhibitor BGB324 partially blocked the activation of HSC by rGAS6 (Fig. 7d). Therefore, we experimentally confirmed the potential contributing role of the GAS6_AXL pair in TCS-induced liver fibrosis, thus leading to increased expression of α-SMA (Fig. 7e).

Overall, our study identified several critical ligand-receptor pairs between the selected crucial subtypes, which are known or have been reported to facilitate liver fibrogenesis. Combing the above results, we delineated the key underlying mechanisms of TCS-induced liver fibrosis (Fig. 7f), which were attributable to cell type-specific modulation on Heps (particularly Hep2 and Hep3), Endos (particularly LSEC_mid2), macrophages (particularly KC_M2 and LCM_M2), B cells (particularly B_plasma) and HSCs (particularly aHSC1).

Discussion

TCS was once considered a safe additive because the median lethal dose (LD$_{50}$) for inducing acute toxicity is as high as 4350 mg/kg body weight in mice and > 5000 mg/kg body weight in dogs [59]. The TCS content in commercial products may reach as high as 17 mmol/L (0.5%) [5]. Although the use of TCS in antiseptic soaps was phased out in the United States in 2016 by FDA, it is still widely used in a wide range of
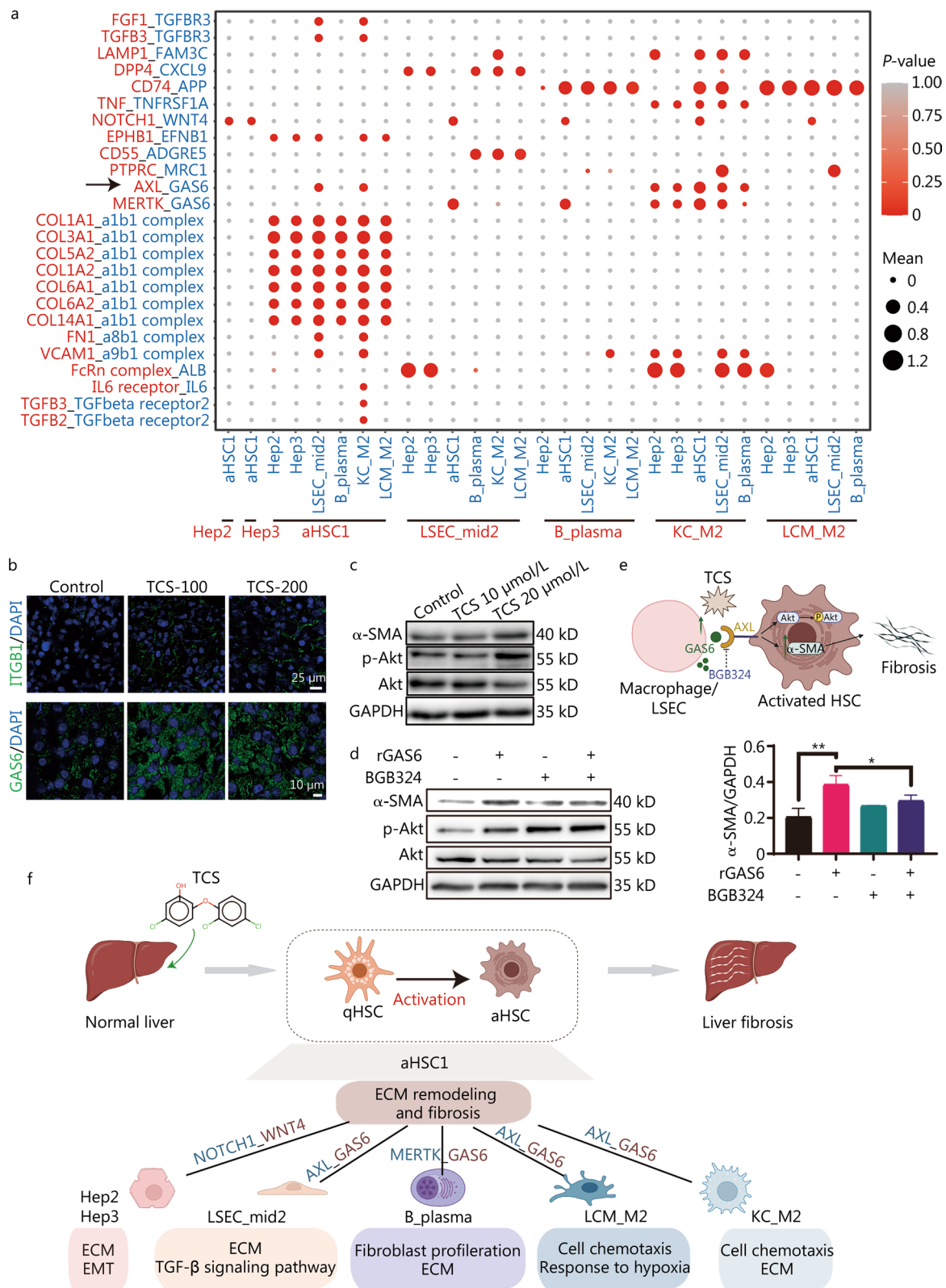
Fig. 7 (See legend on next page.)

Fig. 7 Cell–cell communication crosstalk of different cell types. **a** Dot plot depicting ligand-receptor pairs within different subtypes. Circle sizes indicate mean expression of pairs and colors indicated enrichment of *P*-values in the two subtypes. **b** Immunofluorescence staining of ITGB1 (top) and GAS6 (bottom) on mouse liver frozen sections. Scale bar = 25 µm (top) and scale bar = 10 µm (bottom). **c** LX-2 cells were treated with indicated concentration of TCS for 24 h, and the expression of α-SMA, p-Akt and total Akt were examined with Western blotting, GAPDH was used as loading control. **d** LX-2 cells were incubated with 500 ng/ml rGAS6 for 30 min and/or pre-incubated with BGB324 (1 µmol/L, 30 min), and the expression of α-SMA, p-Akt and total Akt were examined with Western blotting, GAPDH was used as loading control. **e** Scheme showing the potential fibrosis-related mechanism caused by the combination of GAS6 and AXL in HSCs. **f** Summary and inference of cellular communication induced by TCS on mice liver. ITGB1 integrin beta 1, TCS triclosan, α-SMA alpha smooth muscle actin, p-Akt phosphorylated Akt, rGAS6 recombinant GAS6, HSCs hepatic stellate cells, LSEC liver sinusoidal endothelial cells, qHSC quiescent hepatic stellate cells, aHSC activated hepatic stellate cells, ECM extracellular matrix, EMT epithelial-mesenchymal transition; *$P < 0.05$, **$P < 0.01$

personal care and health care products (such as toothpaste, mouthwash, shampoo, deodorant and cosmetics) in many countries [60–63]. The wide use and chemical persistence of TCS have also led to substantial accumulation in the environment, thus causing severe pollution problems [64, 65].

The toxicity of TCS has been studied in different mouse models with varying dosages or exposure terms. For instance, Wang et al. [23] have demonstrated that TCS induces mouse liver tumors through the chimeric antigen receptor (CAR) and PPARα activation at doses of 0, 10, 100 and 200 mg/kg for 14 or 28 d. Cao et al. [42] have examined dose–response genotoxicity of TCS in mice at doses of 0 to 1000 mg/(kg·d) for 19 d. In the present study, we treated mice with 200 mg/(kg·d) body weight for 14 d by oral gavage, and we provide the first detailed single cell atlas in mouse liver with a focus on the TCS-induced liver fibrosis. Of note, although the dosage used in our study was higher than the typical concentrations in consumer products for daily use, the measured TCS serum concentration was largely within the range of reported human body burden levels (i.e., sub µmol/L in serum), and the mice showed no changes in body weight, or in a panel of blood or serum biomarkers. Nevertheless, liver hypertrophy and pathology were observed after the 14-day treatment, thus confirming prior findings indicating that the liver is the main target organ of TCS [11]. Our study exploited scRNA-seq to illustrate TCS treatment-induced modulation of gene expression in major cell types including Heps, HSCs, Endos, lymphocytes and myeloid cells, and their communication crosstalk. More importantly, the molecular and cellular events underlying TCS-induced liver fibrogenesis were dissected at the single cell level.

TCS has been reported to induce an increase in hepatocyte DNA synthesis and cell proliferation. In our study, Heps in the TCS treatment group exhibited obvious proliferation, mainly driven by Hep2 and Hep3 subtypes. In addition, elevated collagen accumulation was observed after TCS treatment, as verified with Masson's trichrome and Sirius red staining, as well as immunoblotting and immunofluorescence experiments. The analysis of subtypes suggested their transition from metabolic processes toward proliferation and fibrosis. The Hep2 and Hep3 subtypes were enriched in ECM and EMT related processes, which might be regulated by TFs such as Gata2 and Mef2c.

Activated HSCs are known as the main ECM-producing cells. The transition from quiescence led to two different trajectories: one subtype participated in cell migration, and the other participated in ECM organization. Recently, Zhang et al. [66] have discovered two major trajectories during HSC activation in liver fibrogenesis, from proliferation to either an inflammatory cluster or collagen organization cluster. Notably, we extended the trajectory starting from quiescent HSCs and accompanied by the activated proliferation subtypes.

Other cells, including Endos and immune cells, also regulate the ECM and contribute to the progression of liver fibrosis. LSECs are specialized Endos that form hepatic sinusoids, which lack a basement membrane, thus allowing for solute exchange between the sinusoid lumen and the space of Disse [67]. In the normal liver, Endos remove circulating antigens and toxins via endocytic receptors, and respond to increased shear stress to maintain normal vascular conditions. Our study suggested that TCS treatment induced disorder in endocytosis and dysfunction in vascular regulation, which are the representative features of endothelial dysfunction observed in cirrhosis [68]. During the progression of liver fibrosis, LSEC fenestrae are diminished, thus preventing the exchange in substances and oxygen between the liver parenchyma and sinusoidal blood, which is also known as capillarization, thereby leading to a failure in suppressing HSCs [69]. In our study, LSECs exhibited a phenotypic shift to LVECs, in line with the capillarization features. Furthermore, LSEC_mid2 cells were charactered by middle-zone markers and overexpression of genes associated with ECM and TGF-β signaling pathway. This might be regulated by TF Hlf, which facilitates liver fibrosis through activation of HSCs driven by the HLF/IL-6/STAT3 feedforward circuit [70].

Studies have shown that B cells are required for liver fibrogenesis in an antibody- and T cell-independent

manner [71]. Our study revealed that the pro-fibrogenesis function of B cells appeared to be mainly related to the plasma cell, which sharply increased after TCS treatment. The relationship between plasma cells and stellate cells in autoimmune hepatitis has been established, exhibiting co-localization and positive correlation [72]. In agreement with this relationship, genes associated with ECM organization, response to hypoxia and tissue remodeling were up-regulated in plasma cells in our data.

Among myeloid cells, macrophages, including LCM and Kupffer cells, displayed M2-skewed phenotype. M2 macrophages release anti-inflammatory or pro-resolving mediators, which influence wound repair, tissue remodeling and fibrosis [73]. Several up-regulated genes facilitating liver fibrosis were identified in our data. For example, *Il1b* is a potent inflammatory cytokine produced mainly by macrophages that participate in toxic-, ethanol- and NASH-induced fibrosis [74, 75], and it has been found to prolong the survival of HSCs [76]. *Il6* is a key pro-inflammatory and profibrogenic cytokine that drives liver fibrosis [57]. *Mmp2* belongs to the matrix metalloproteinase family, and its increased expression has been found to promote ECM deposition [77]. Additionally, *Ppara*, a nuclear receptor participating in the development of hepatic steatosis induced by TCS [21], was up-regulated after TCS treatment in LSEC_mid2, Hep3, aHSC1 and KC_M2 cells in our study.

Finally, cell–cell communication crosstalk analysis confirmed the central role of HSCs in association with other cell types. Notably, aHSC1 cells exhibited the most interactions with other subtypes when acting as either source or target in ligand-receptor pairing. The combination of GAS6 and AXL was verified to increase the expression of α-SMA and promote fibrosis, collagen molecules and the corresponding complex, IL6 receptor_IL6, TGFB2/3_TGFbeta receptor2/3, MERTK_GAS6 and TNF_TNFRSF1A, in line with the role of aHSC1 as a major executor of fibrogenesis.

Conclusions

The present study provides the first comprehensive analysis of cellular and biological processes involved in TCS-induced hepatotoxicity through scRNA-seq. Our analysis uncovered the molecular changes in the six main liver cell types, and enabled the construction of an interaction network of cells centering on the activation of HSCs. Our study suggests that TCS modulates different cell types in concert to activate HSCs, promoting fibrogenesis and resulting in hepatotoxicity.

Abbreviations

aHSC	Activated hepatic stellate cells
AUC	Area under the curve
BEAM	Branched expression analysis modeling
CAR	Chimeric antigen receptor
CCK-8	Cell counting kit-8
DEGs	Differentially expressed genes
DEMs	Differentially expressed metabolites
DEPs	Differentially expressed proteins
DES	Desmin
DIA	Data-independent acquisition
DTT	DL-Dithiothreitol
ECM	Extracellular matrix
EMT	Epithelial-mesenchymal transition
Endos	Endothelial cells
FDA	Food and Drug Administration
FDR	False discovery rate
GAS6	Growth arrest specific 6
GO	Gene ontology
GSVA	Gene set variation analysis
H&E	Hematoxylin and eosin
Heps	Hepatocytes
HSCs	Hepatic stellate cells
IAA	Iodoacetamide
ITGB1	Integrin subunit beta 1
KEGG	Kyoto Encyclopedia of Genes and Genomes
LC–MS/MS	Liquid chromatography tandem–mass spectrometry
LCMs	Liver capsular macrophages
LD_{50}	Median lethal dose
LSECs	Liver sinusoidal endothelial cells
LVECs	Liver vascular endothelial cells
LYVE1	Lymphatic vessel endothelial hyaluronan receptor 1
NASH	Nonalcoholic steatohepatitis
NK	Natural killer cells
p-Akt	Phosphorylated Akt
pDCs	Plasmacytoid dendritic cells
PLS-DA	Partial least squares discriminant analysis
PPARα	Peroxisome proliferator activated receptor α
Prolif	Proliferative cells
qHSC	Quiescent hepatic stellate cells
rGAS6	Recombinant GAS6
RSS	Regulon specificity score
RT	Room temperature
scRNA-seq	Single cell RNA sequencing
SDC	Sodium deoxycholate
STAR	Spliced Transcripts Alignment to a Reference
TCS	Triclosan
TF	Transcription factor
UMAP	Uniform manifold approximation and projection for dimension reduction
UMI	Unique molecular identifier
α-SMA	Alpha smooth muscle actin

Supplementary Information

Additional file 1: Fig. S1. TCS showed no signs of severe toxicity. **Fig. S2.** The XIC (**a**) and mass spectrogram (**b**) of TCS detected in LC–MS/MS. **Fig. S3.** Data distribution after quality control (feature number between 200 and 5000; UMI count between 500 and 20,000; and mitochondrial gene percentage below 0.15 or 0.25) in each sample, and a total of 76,209 cells (37,841 for the control group and 38,368 for TCS-200 group) remained for further analysis. **Fig. S4.** Heatmap showed top 10 DEGs of each cell type based on the average fold change value. **Fig. S5.** Cellular change of hepatocytes (Heps). **Fig. S6.** Cellular change of HSCs. **Fig. S7.** Functions/processes enriched in down-regulated (left) and up-regulated (right) DEGs after TCS treatment in Endos. **Fig. S8.** Emergence of diverse macrophages after TCS treatment. **Fig. S9.** Cell–cell communication change after TCS treatment.

Bai *et al. Military Medical Research*   (2023) 10:7

Page 20 of 22

Declarations

Ethics approval and consent to participate
All animal experimental procedures were approved by the Animal Care and Use Committee at Shenzhen People's Hospital (AUP-210901-DLY-0001-01).

Consent for publication
Not applicable.

Competing interests
The authors declare that they have no competing interests.

Author details
[1]Department of Nephrology, Shenzhen Key Laboratory of Kidney Diseases, and Shenzhen Clinical Research Centre for Geriatrics, Shenzhen People's Hospital, the First Affiliated Hospital, Southern University of Science and Technology, Shenzhen 518020, China. [2]Department of Urology, Shenzhen People's Hospital, the First Affiliated Hospital, Southern University Science and Technology, the Second Clinical Medical College, Jinan University, Shenzhen 518020, China. [3]Integrated Chinese and Western Medicine Postdoctoral Research Station, Jinan University, Guangzhou 510632, China. [4]Artemisinin Research Center, and Institute of Chinese Materia Medica, China Academy of Chinese Medical Sciences, Beijing 100700, China. [5]Guangdong Provincial Key Laboratory of New Drug Screening, School of Pharmaceutical Sciences, Southern Medical University, Guangzhou 510515, China. [6]Center for Reproductive Medicine, Dongguan Maternal and Child Health Care Hospital, Southern Medical University, Dongguan 523125, Guangdong, China.

References
1. Yueh MF, Tukey RH. Triclosan: a widespread environmental toxicant with many biological effects. Annu Rev Pharmacol Toxicol. 2016;56:251–72.
2. Rodricks JV, Swenberg JA, Borzelleca JF, Maronpot RR, Shipp AM. Triclosan: a critical review of the experimental data and development of margins of safety for consumer products. Crit Rev Toxicol. 2010;40(5):422–84.
3. FDA. FDA issues final rule on safety and effectiveness of consumer hand sanitizers. 2019. https://www.fda.gov/news-events/press-announcements/fda-issues-final-rule-safety-and-effectiveness-consumer-hand-sanitizers.
4. Lee JD, Lee JY, Kwack SJ, Shin CY, Jang HJ, Kim HY, et al. Risk assessment of triclosan, a cosmetic preservative. Toxicol Res. 2019;35(2):137–54.
5. Weatherly LM, Gosse JA. Triclosan exposure, transformation, and human health effects. J Toxicol Environ Health B Crit Rev. 2017;20(8):447–69.
6. Ashley-Martin J, Dodds L, Arbuckle TE, Marshall J. Prenatal triclosan exposure and cord blood immune system biomarkers. Int J Hyg Environ Health. 2016;219(4–5):454–7.
7. Bever CS, Rand AA, Nording M, Taft D, Kalanetra KM, Mills DA, et al. Effects of triclosan in breast milk on the infant fecal microbiome. Chemosphere. 2018;203:467–73.
8. Yin J, Wei L, Shi Y, Zhang J, Wu Q, Shao B. Chinese population exposure to triclosan and triclocarban as measured via human urine and nails. Environ Geochem Health. 2016;38(5):1125–35.
9. Allmyr M, Panagiotidis G, Sparve E, Diczfalusy U, Sandborgh-Englund G. Human exposure to triclosan via toothpaste does not change CYP3A4 activity or plasma concentrations of thyroid hormones. Basic Clin Pharmacol Toxicol. 2009;105(5):339–44.
10. Lin YJ. Buccal absorption of triclosan following topical mouthrinse application. Am J Dent. 2000;13(4):215–7.
11. Geens T, Neels H, Covaci A. Distribution of bisphenol-A, triclosan and n-nonylphenol in human adipose tissue, liver and brain. Chemosphere. 2012;87(7):796–802.
12. Wu Y, Chitranshi P, Loukotková L, Gamboa Da Costa G, Beland FA, Zhang J, et al. Cytochrome P450-mediated metabolism of triclosan attenuates its cytotoxicity in hepatic cells. Arch Toxicol. 2017;91(6):2405–23.
13. Wilburn WJ, Jamal S, Ismail F, Brooks D, Whalen M. Evaluation of triclosan exposures on secretion of pro-inflammatory cytokines from human immune cells. Environ Toxicol Pharmacol. 2021;83:103599.
14. Ruszkiewicz JA, Li S, Rodriguez MB, Aschner M. Is triclosan a neurotoxic agent? J Toxicol Environ Health B Crit Rev. 2017;20(2):104–17.
15. Halden RU, Lindeman AE, Aiello AE, Andrews D, Arnold WA, Fair P, et al. The florence statement on triclosan and triclocarban. Environ Health Perspect. 2017;125(6):064501.
16. Sanidad KZ, Xiao H, Zhang G. Triclosan, a common antimicrobial ingredient, on gut microbiota and gut health. Gut Microbes. 2019;10(3):434–7.
17. Yang H, Wang W, Romano KA, Gu M, Sanidad KZ, Kim D, et al. A common antimicrobial additive increases colonic inflammation and colitis-associated colon tumorigenesis in mice. Sci Transl Med. 2018;10(443):eaan4116.
18. Tabari SA, Esfahani ML, Hosseini SM, Rahimi A. Neurobehavioral toxicity of triclosan in mice. Food Chem Toxicol. 2019;130:154–60.
19. Hao Y, Meng L, Zhang Y, Chen A, Zhao Y, Lian K, et al. Effects of chronic triclosan exposure on social behaviors in adult mice. J Hazard Mater. 2021;424(Pt C):127562.
20. Cai S, Zhu J, Sun L, Fan C, Zhong Y, Shen Q, et al. Association between urinary triclosan with bone mass density and osteoporosis in US adult women, 2005–2010. J Clin Endocrinol Metab. 2019;104(10):4531–8.
21. Yueh MF, He F, Chen C, Vu C, Tripathi A, Knight R, et al. Triclosan leads to dysregulation of the metabolic regulator FGF21 exacerbating high fat diet-induced nonalcoholic fatty liver disease. Proc Natl Acad Sci U S A. 2020;117(49):31259–66.
22. Yueh MF, Taniguchi K, Chen S, Evans RM, Hammock BD, Karin M, et al. The commonly used antimicrobial additive triclosan is a liver tumor promoter. Proc Natl Acad Sci U S A. 2014;111(48):17200–5.
23. Wang Z, Li X, Klaunig JE. Investigation of the mechanism of triclosan induced mouse liver tumors. Regul Toxicol Pharmacol. 2017;86:137–47.
24. Tang Y, Vanlandingham MM, Wu Y, Beland FA, Olson GR, Fang JL. Role of peroxisome proliferator-activated receptor alpha (PPARα) and

Bai *et al. Military Medical Research*   (2023) 10:7

Page 21 of 22

PPARα-mediated species differences in triclosan-induced liver toxicity. Arch Toxicol. 2018;92(11):3391–402.

25. Huang W, Xie P, Cai Z. Lipid metabolism disorders contribute to hepatotoxicity of triclosan in mice. J Hazard Mater. 2020;384:121310.

26. Xie T, Wang Y, Deng N, Huang G, Taghavifar F, Geng Y, et al. Single-cell deconvolution of fibroblast heterogeneity in mouse pulmonary fibrosis. Cell Rep. 2018;22(13):3625–40.

27. Wang JJ, Tian Y, Li MH, Feng YQ, Kong L, Zhang FL, et al. Single-cell transcriptome dissection of the toxic impact of Di (2-ethylhexyl) phthalate on primordial follicle assembly. Theranostics. 2021;11(10):4992–5009.

28. Brenner E, Tiwari GR, Kapoor M, Liu Y, Brock A, Mayfield RD. Single cell transcriptome profiling of the human alcohol-dependent brain. Hum Mol Genet. 2020;29(7):1144–53.

29. Ramachandran P, Dobie R, Wilson-Kanamori JR, Dora EF, Henderson BEP, Luu NT, et al. Resolving the fibrotic niche of human liver cirrhosis at single-cell level. Nature. 2019;575(7783):512–8.

30. Zhang H, Ma Y, Cheng X, Wu D, Huang X, Chen B, et al. Targeting epigenetically maladapted vascular niche alleviates liver fibrosis in nonalcoholic steatohepatitis. Sci Transl Med. 2021;13(614):eabd1206.

31. Wu SZ, Al-Eryani G, Roden DL, Junankar S, Harvey K, Andersson A, et al. A single-cell and spatially resolved atlas of human breast cancers. Nat Genet. 2021;53(9):1334–47.

32. Brancale J, Vilarinho S. A single cell gene expression atlas of 28 human livers. J Hepatol. 2021;75(1):219–20.

33. Yu G, Wang LG, Han Y, He QY. clusterProfiler: an R package for comparing biological themes among gene clusters. OMICS. 2012;16(5):284–7.

34. Hanzelmann S, Castelo R, Guinney J. GSVA: gene set variation analysis for microarray and RNA-seq data. BMC Bioinform. 2013;14:7.

35. Aibar S, Gonzalez-Blas CB, Moerman T, Huynh-Thu VA, Imrichova H, Hulselmans G, et al. SCENIC: single-cell regulatory network inference and clustering. Nat Methods. 2017;14(11):1083–6.

36. Shannon P, Markiel A, Ozier O, Baliga NS, Wang JT, Ramage D, et al. Cytoscape: a software environment for integrated models of biomolecular interaction networks. Genome Res. 2003;13(11):2498–504.

37. Trapnell C, Cacchiarelli D, Grimsby J, Pokharel P, Li S, Morse M, et al. The dynamics and regulators of cell fate decisions are revealed by pseudotemporal ordering of single cells. Nat Biotechnol. 2014;32(4):381–6.

38. La Manno G, Soldatov R, Zeisel A, Braun E, Hochgerner H, Petukhov V, et al. RNA velocity of single cells. Nature. 2018;560(7719):494–8.

39. Bergen V, Lange M, Peidli S, Wolf FA, Theis FJ. Generalizing RNA velocity to transient cell states through dynamical modeling. Nat Biotechnol. 2020;38(12):1408–14.

40. Efremova M, Vento-Tormo M, Teichmann SA, Vento-Tormo R. Cell PhoneDB: inferring cell-cell communication from combined expression of multi-subunit ligand-receptor complexes. Nat Protoc. 2020;15(4):1484–506.

41. Guo X, Zhang Y, Zheng L, Zheng C, Song J, Zhang Q, et al. Global characterization of T cells in non-small-cell lung cancer by single-cell sequencing. Nat Med. 2018;24(7):978–85.

42. Cao Y, Xi J, You X, Liu W, Luan Y. Dose-response genotoxicity of triclosan in mice: an estimate of acceptable daily intake based on organ toxicity. Toxicol Res (Camb). 2021;10(6):1153–61.

43. Lentjes MH, Niessen HE, Akiyama Y, De Bruine AP, Melotte V, Van Engeland M. The emerging role of GATA transcription factors in development and disease. Expert Rev Mol Med. 2016;18:e3.

44. Pon JR, Marra MA. MEF2 transcription factors: developmental regulators and emerging cancer genes. Oncotarget. 2016;7(3):2297–312.

45. Schulien I, Hockenjos B, Schmitt-Graeff A, Perdekamp MG, Follo M, Thimme R, et al. The transcription factor c-Jun/AP-1 promotes liver fibrosis during non-alcoholic steatohepatitis by regulating Osteopontin expression. Cell Death Differ. 2019;26(9):1688–99.

46. Rao S, Yang X, Ohshiro K, Zaidi S, Wang Z, Shetty K, et al. β2-spectrin (SPTBN1) as a therapeutic target for diet-induced liver disease and preventing cancer development. Sci Transl Med. 2021;13(624):eabk2267.

47. Su T, Yang Y, Lai S, Jeong J, Jung Y, Mcconnell M, et al. Single-cell transcriptomics reveals zone-specific alterations of liver sinusoidal endothelial cells in cirrhosis. Cell Mol Gastroenterol Hepatol. 2021;11(4):1139–61.

48. Poisson J, Lemoinne S, Boulanger C, Durand F, Moreau R, Valla D, et al. Liver sinusoidal endothelial cells: physiology and role in liver diseases. J Hepatol. 2017;66(1):212–27.

49. Chen L, Gu T, Li B, Li F, Ma Z, Zhang Q, et al. Delta-like ligand 4/DLL4 regulates the capillarization of liver sinusoidal endothelial cell and liver fibrogenesis. Biochim Biophys Acta Mol Cell Res. 2019;1866(10):1663–75.

50. Bhogal RK, Bona CA. B cells: no longer bystanders in liver fibrosis. J Clin Invest. 2005;115(11):2962–5.

51. Doherty DG. Immunity, tolerance and autoimmunity in the liver: a comprehensive review. J Autoimmun. 2016;66:60–75.

52. Zheng S, Zhang P, Chen Y, Zheng S, Zheng L, Weng Z. Inhibition of Notch signaling attenuates schistosomiasis hepatic fibrosis via blocking macrophage M2 polarization. PLoS ONE. 2016;11(11):e0166808.

53. Xu L, Chen Y, Nagashimada M, Ni Y, Zhuge F, Chen G, et al. CC chemokine ligand 3 deficiency ameliorates diet-induced steatohepatitis by regulating liver macrophage recruitment and M1/M2 status in mice. Metabolism. 2021;125:154914.

54. Weiskirchen R, Tacke F. Liver fibrosis: from pathogenesis to novel therapies. Dig Dis. 2016;34(4):410–22.

55. Xiong X, Kuang H, Ansari S, Liu T, Gong J, Wang S, et al. Landscape of intercellular crosstalk in healthy and NASH liver revealed by single-cell secretome gene analysis. Mol Cell. 2019;75(3):644–60.

56. Cai B, Dongiovanni P, Corey KE, Wang X, Shmarakov IO, Zheng Z, et al. Macrophage MerTK promotes liver fibrosis in nonalcoholic steatohepatitis. Cell Metab. 2020;31(2):406–21.

57. Kisseleva T, Brenner D. Molecular and cellular mechanisms of liver fibrosis and its regression. Nat Rev Gastroenterol Hepatol. 2021;18(3):151–66.

58. Bárcena C, Stefanovic M, Tutusaus A, Joannas L, Menéndez A, García-Ruiz C, et al. Gas6/Axl pathway is activated in chronic liver disease and its targeting reduces fibrosis via hepatic stellate cell inactivation. J Hepatol. 2015;63(3):670–8.

59. Fang JL, Stingley RL, Beland FA, Harrouk W, Lumpkins DL, Howard P. Occurrence, efficacy, metabolism, and toxicity of triclosan. J Environ Sci Health C Environ Carcinog Ecotoxicol Rev. 2010;28(3):147–71.

60. Lu S, Wang B, Xin M, Wang J, Gu X, Lian M, et al. Insights into the spatiotemporal occurrence and mixture risk assessment of household and personal care products in the waters from rivers to Laizhou Bay, southern Bohai Sea. Sci Total Environ. 2022;810:152290.

61. Dix-Cooper L, Kosatsky T. Use of antibacterial toothpaste is associated with higher urinary triclosan concentrations in Asian immigrant women living in Vancouver, Canada. Sci Total Environ. 2019;671:897–904.

62. Vindenes HK, Svanes C, Lygre SHL, Real FG, Ringel-Kulka T, Bertelsen RJ. Exposure to environmental phenols and parabens, and relation to body mass index, eczema and respiratory outcomes in the Norwegian RHINESSA study. Environ Health. 2021;20(1):81.

63. Ewg. Where is triclosan still approved for use. 2017. https://www.ewg.org/consumer-guides/where-triclosan-still-approved-use.

64. Milanović M, Đurić L, Milošević N, Milić N. Comprehensive insight into triclosan-from widespread occurrence to health outcomes. Environ Sci Pollut Res Int. 2021. https://doi.org/10.1007/s11356-021-17273-0:1-22.

65. Tong H, Hu X, Zhong X, Jiang Q. Adsorption and desorption of triclosan on biodegradable polyhydroxybutyrate microplastics. Environ Toxicol Chem. 2021;40(1):72–8.

66. Zhang W, Conway SJ, Liu Y, Snider P, Chen H, Gao H, et al. Heterogeneity of hepatic stellate cells in fibrogenesis of the liver: insights from single-cell transcriptomic analysis in liver injury. Cells. 2021;10(8):2129.

67. Seki E, Schwabe RF. Hepatic inflammation and fibrosis: functional links and key pathways. Hepatology. 2015;61(3):1066–79.

68. Iwakiri Y. Endothelial dysfunction in the regulation of cirrhosis and portal hypertension. Liver Int. 2012;32(2):199–213.

69. Xie G, Wang X, Wang L, Wang L, Atkinson RD, Kanel GC, et al. Role of differentiation of liver sinusoidal endothelial cells in progression and regression of hepatic fibrosis in rats. Gastroenterology. 2012;142(4):918-27.e6.

70. Xiang DM, Sun W, Ning BF, Zhou TF, Li XF, Zhong W, et al. The HLF/IL-6/STAT3 feedforward circuit drives hepatic stellate cell activation to promote liver fibrosis. Gut. 2018;67(9):1704–15.

71. Novobrantseva TI, Majeau GR, Amatucci A, Kogan S, Brenner I, Casola S, et al. Attenuated liver fibrosis in the absence of B cells. J Clin Invest. 2005;115(11):3072–82.

72. Brandao DF, Ramalho FS, Martinelli AL, Zucoloto S, Ramalho LN. Relationship between plasma cells and hepatic stellate cells in autoimmune hepatitis. Pathol Res Pract. 2010;206(12):800–4.

Bai *et al. Military Medical Research*　(2023) 10:7

Page 22 of 22

73. Sun YY, Li XF, Meng XM, Huang C, Zhang L, Li J. Macrophage phenotype in liver injury and repair. Scand J Immunol. 2017;85(3):166–74.

74. Miura K, Kodama Y, Inokuchi S, Schnabl B, Aoyama T, Ohnishi H, et al. Toll-like receptor 9 promotes steatohepatitis by induction of interleukin-1beta in mice. Gastroenterology. 2010;139(1):323–34.

75. Iannitti RG, Napolioni V, Oikonomou V, Luca AD, Galosi C, Pariano M, et al. IL-1 receptor antagonist ameliorates inflammasome-dependent inflammation in murine and human cystic fibrosis. Nat Commun. 2016;7:10791.

76. Pradere JP, Kluwe J, De Minicis S, Jiao JJ, Gwak GY, Dapito DH, et al. Hepatic macrophages but not dendritic cells contribute to liver fibrosis by promoting the survival of activated hepatic stellate cells in mice. Hepatology. 2013;58(4):1461–73.

77. Robert S, Gicquel T, Victoni T, Valenca S, Barreto E, Bailly-Maitre B, et al. Involvement of matrix metalloproteinases (MMPs) and inflammasome pathway in molecular mechanisms of fibrosis. Biosci Rep. 2016;36(4):e00360.